Differences in an aversive teaching signal produce brainwide and behavioral substrates of susceptibility

Anna Zhukovskaya[1], Christopher A. Zimmerman[1], Lindsay Willmore[1], Sanjeev N. Janarthanan[1], Annegret L. Falkner[1], Ilana B. Witten*[1]

[1] Princeton Neuroscience Institute, Princeton University, Princeton NJ 08544 USA

*Address correspondence to iwitten@princeton.edu

Some individuals are susceptible to the experience of chronic stress and others are more resilient. While many brain regions implicated in learning are dysregulated after stress, little is known about whether and how neural teaching signals during stress differ between susceptible and resilient individuals. Here, we seek to determine if activity in the lateral habenula (LHb), which encodes a negative teaching signal, differs between stress susceptible and resilient mice during stress to produce different outcomes. After but not before chronic social defeat stress (CSDS), the LHb is active when susceptible mice are in the proximity of the aggressor strain. During stress itself, LHb activity is higher in susceptible mice during aggressor proximity, and stimulation of the LHb during stress biases mice towards susceptibility. This stimulation generates a persistent and widespread increase in the balance of subcortical versus cortical activity that closely mimics the brainwide correlates of susceptibility. Taken together, our results indicate that a stronger aversive teaching signal in the LHb during stress produces brainwide and behavioral substrates of susceptibility.

Introduction

Chronic stress increases the risk of developing mental illness[1–3]. However, some individuals are more susceptible to the adverse effects of chronic stress, whereas others are more resilient. Pioneering work has used chronic social defeat stress (CSDS) to model this variability in rodents[4–13]. This prior work has largely focused on identifying the factors that predispose to susceptibility to stress[14–19], or on identifying the changes in the brain after stress[4,5,10,11,20–25]. However, the question of how activity differs between susceptible and resilient individuals during stress itself in order to lead to different stress outcomes remains largely unaddressed.

To begin to address this, we recently developed approaches to automatically identify relevant behaviors during social defeat from video recordings (e.g. being attacked, fighting back)[26]. Using these tools, we observed distinct neural correlates in the midbrain dopamine system (a key component of the brain's positive reinforcement system[27–31]) across resilient and susceptible mice: more dopamine neuron activity during an “active coping” strategy (i.e. fighting back behavior) in resilient mice, and more dopamine during escape in susceptible animals. Together, this may help explain how individuals develop resilient versus susceptible strategies. However, these differences in the dopamine system between resilient and susceptible mice emerge gradually across the ten days of defeat, leaving open the question of if there are important differences in other populations that emerge earlier.

Given that stressors have negative valence, we hypothesize that differences in the aversive learning system may be present earlier during stress and be critical to the formation of the susceptible state. The lateral habenula (LHb) is a key region for aversive learning. It encodes a negative reward prediction error[32–34], drives aversive learning[35,36], and is dysregulated by stress[20,37–45]. However, if and when the LHb first responds differentially to stressors in susceptible versus resilient individuals, and whether such differences are causal to the development of the susceptible state, remains unknown.

To address this, we recorded longitudinally from the LHb before, during, and after CSDS, and found elevated activity in the LHb in susceptible mice starting on the first day of stress. To determine if these differences in the LHb between susceptible and resilient mice are causal to susceptibility, we activated the LHb during defeat stress, which biased animals towards the susceptible phenotype. Finally, we examined the effects of LHb activity during defeat on brainwide activity. LHb activation generated a sustained increase in the balance of subcortical versus cortical activity that closely matched the pattern found in susceptible mice. Thus, heightened LHb activity during stress is present in susceptible mice and produces brainwide and behavioral correlates of susceptibility.

Results

CSDS produces strain-specific social aversion and anxiety-like behaviors

Male mice underwent 10 days of chronic social defeat stress (CSDS), where they were defeated by a new aggressor for 5 minutes a day, and housed with the aggressor (who was separated by a barrier) for the remainder of each day (Figure 1A). CSDS was preceded by assays of sociability and followed both by assays of sociability and of anxiety-like behavior (Figure 1B-J, Figure S1A-C). Consistent with previous studies[4,5,9,46,47], a subset of mice showed decreased

social interaction time with the aggressor strain after (but not before) CSDS in a “social interaction” (SI) test when the social target was behind a barrier (Figure 1B, Figure S1A). Mice were defined as susceptible if their social interaction time in the SI test was less than one standard deviation below that of unstressed controls[26]; otherwise, they were considered resilient (Figure S1A).

As expected, susceptibility by this measure correlated with social avoidance of a juvenile of the aggressor strain in a freely moving assay (Figure 1C-D), as well as with higher anxiety-like behavior in non-social settings (elevated plus maze, Figure 1E-F; novelty-suppressed feeding, Figure 1G-H; immobility in a novel context, Figure I-J)[7,8,26,38,48,]. Susceptibility did not generalize to social avoidance of the self strain or a control strain; in fact, susceptible mice preferred their own strain after stress (Figure 1B for SI test; Figure 1C-D for freely moving assay). This observation of strain-specific avoidance learning is consistent with recent work[49,50] (but see [51] which used longer defeat sessions). Thus, in susceptible mice, CSDS produced a generalized anxiety-like phenotype in non-social contexts, while also generating strain-specific social avoidance.

CSDS produces neural correlates of strain-specific aversion in the LHb in susceptible mice

To determine whether neural activity in the lateral habenula (LHb) before and after CSDS relates to the observed strain-specific avoidance learning (Figure 1B, C-D), we used fiber photometry (Figure 2A-H, histology summary: Figure S2A-B) and cellular resolution calcium imaging (Figure 2I-Q, histology summary: Figure S2C) to record responses to the aggressor strain, the defeated mouse’s own strain, and a control strain in the pre- and post-CSDS SI tests. Before CSDS, there was no modulation of the LHb to any strain in either susceptible or resilient mice (fiber photometry: Figure 2D; cellular resolution: Figure 2M, Figure S2D). After CSDS, there was elevated activity in susceptible but not resilient mice, specifically to the aggressor strain (fiber photometry: Figure 2E, F-H; cellular resolution: Figure 2N, O-Q, Figure S2D).

Thus, while social responses before CSDS were not apparent in the LHb in susceptible or resilient mice, stress produced neural correlates of strain-specific aversion in susceptible mice. We next sought to determine how LHb activity relates to behavior during stress itself, and if and when stress-related activity first differed between susceptible and resilient mice.

LHb activity during defeat is elevated during attacks and other proximal behaviors

We performed high-speed, multiview videography during each defeat session, followed by automated behavioral quantification (Figure 3A). Key points in both mice were tracked (Figure 3A) and used to define 12 features - such as relative orientation and distance between the mice - to capture the postures, positions and movements of the animals (Figure 3B; see Methods for explanation of feature calculation). These features from each frame were then embedded into a 2D *t*-distributed stochastic neighbor embedding (*t*-SNE) manifold (Figure 3C, Figure S3A), which was followed by density-based clustering to define distinct social and non-social behaviors[26]. Clusters were numbered by proximity between the mice.

Average neural activity from the fiber photometry recordings in LHb was plotted in the *t*-SNE space (Figure 3D, results split across cohorts in: Figure S3B; see Methods). Activity was greatest for clusters that corresponded to high proximity between the mice (Figure 3E, F), consistent with the aversive nature of being near the aggressor.

To better interpret these proximal clusters, we trained random forest classifiers[26] to identify four behaviors - being investigated, being attacked, fighting back, and fleeing (Figure S3C, D) - across all video frames using the same 12 features as were embedded into *t*-SNE space (Figure 3B). These four behaviors together spanned the portion of the *t*-SNE map where LHb activity was the highest (compare Figure 3G-J for random forest densities with Figure 3D for neural data). The onset of these four behaviors had similar responses (Figure 3K-N).

Taken together, this implies that LHb is elevated across proximal behaviors during defeat, with little differentiation across such behaviors. This lack of behavioral differentiation contrasts with our observations in VTA dopamine neurons, as in that case we saw different response patterns in relation to different behaviors (e.g. flee versus fight back)[26].

From the first defeat session, LHb activity is higher in susceptible mice when attacked

Thus far, we observed differences in LHb activity in susceptible and resilient mice following but not preceding CSDS (Figure 2), as well as elevated activity during proximal behaviors across all mice during defeat (Figure 3). We next asked whether neural activity in LHb is different between susceptible and resilient mice during defeat, and if so, when differences first emerged.

Susceptible mice had higher activity than resilient mice in the portion of the *t*-SNE space corresponding to proximal behaviors such as being attacked, fighting, or fleeing (Figure 4A-C; compare to random forest densities in Figure 3G-J; consistent pattern across 2 cohorts: Figure S4A-B). In contrast, resilient mice had higher activity in the portion of the *t*-SNE map corresponding to a vigilance-like posture (Figure 4C; close to a wall, low body posture, and oriented toward the aggressor: Figure S4C-H). These conclusions were also evident from directly time-locking activity to the random-forest identified behaviors (Figure 4D-G).

Rather than emerging gradually, these differences between susceptible and resilient mice were present from the first day of CSDS (Figure 4H-O; analogous results from *t*-SNE in Figure S4I). These differences imply that heightened initial LHb responses to the stressor might produce susceptibility. This also provides a clear contrast to our prior observations in the VTA dopamine system, where we observed differences in neural correlates in susceptible and resilient mice emerge gradually over the course of CSDS[26].

Closed-loop stimulation of the LHb during defeat biases towards susceptibility

To determine if the elevated activity in the LHb observed in susceptible mice during defeat causes susceptibility, we performed closed-loop optogenetic stimulation during defeat. vGlut2-Cre males were bilaterally injected in the LHb with either a Cre-dependent excitatory opsin (ChR2 or ChRmine) or control virus (YFP), and optical fibers were implanted in the LHb (Figure 5A, histology: Figure S5A).

In order to recapitulate the heightened LHb activity during attack, fighting, and fleeing observed in susceptible mice (Figure 5D-F), we streamed video frames to our pose-estimation network, calculated the 12 features as previously described (Figure 3B), and inputted them into the random forest classifier to identify attack and trigger laser stimulation[26] (Figure 5B). Post-hoc analyses confirmed that this resulted in the greatest stimulation during attack (Figure 5C-E), as well as stimulation during fighting and fleeing which closely follow attack (Figure 5E, compare to susceptible mice LHb activity map in Figure 4B). Across the 10 days of CSDS, the average duration of this stimulation was ~1.07 min/day (21.4% of session; Figure 5F).

The stimulation of the LHb biased towards a susceptible phenotype. Specifically, mice that received stimulation were less social on the SI test (Figure 5G), spent less time in the open arms in the elevated plus maze (Figure 5H), and less time in the center of the open field (Figure 5I). This difference was not due to significant differences in being attacked across the groups (Figure S5B).

Stimulation of the LHb during defeat produces durable, brainwide changes in the balance of neural activation of subcortical versus cortical networks

Stimulation of the LHb during defeat produced susceptibility (Figure 5). What downstream changes in neural activity might underlie this, and how do such changes relate to the neural substrates of susceptibility?

To address these questions, we performed high resolution and high signal-to-noise measurements of brainwide activation in mice that had received attack-triggered LHb stimulation during defeat or YFP control mice who also underwent defeat (Figure 6A). Approximately a week after the last day of CSDS, and an hour before sacrificing, each mouse was introduced for 10 minutes to the cage of a novel aggressor restrained under a mesh cup (Figure 6B). We next cleared the brains with iDISCO+, stained for the immediate early gene Fos as a marker of neural activation, and imaged with a dynamic axial sweeping light sheet fluorescence microscope (Figure 6C)[52,53]. We then used an automated deep learning-assisted cell detection pipeline[54] to generate cellular resolution maps of brainwide neural activation registered to the Allen common coordinate framework (CCF)[55] for each animal (Figure 6C, D; see Methods).

We first analyzed how the brainwide response to the aggressor differed across resilient and susceptible mice. A generalized linear model (GLM) was used to estimate the contribution of SI time, as a proxy of susceptibility versus resilience, to neural activation (Fos^+ cell counts) for each brain region, while accounting for the total Fos count in each sample (see Methods). This revealed that activation of a surprisingly large fraction of regions was significantly modulated by susceptibility versus resilience — approximately 30% of all brain regions (61/200; 10% false discovery rate; Figure 6E; Supplementary Data Table 14).

A striking pattern was evident when visualizing the difference in neural activation (Fos^+ cell density) across the brain in resilient versus susceptible mice: resilient mice had stronger neural activation in cortical regions, whereas susceptible mice had stronger neural activation in subcortical nuclei (Figure 6D, middle row; interactive visualization of 3,246,281 Fos^+ cells across the brain: https://www.brainsharer.org/ng/?id=876). For example, in resilient mice there was more activity in the anterior cingulate cortex (both dorsal and ventral; $p < 0.001$), motor cortex (secondary motor area; $p < 0.01$) and sensory cortices (anteromedial visual area, primary somatosensory area barrel field, piriform cortex, among others; $p < 0.001$, see Supplementary Data Table 14 for effect sizes and statistics). In contrast, in susceptible mice there was more activity in the parabrachial nucleus, pedunculopontine nucleus, substantia nigra pars reticulata, medial habenula, and central and lateral amygdala ($p < 0.001$ for all; see Supplementary Data Table 14 for effect sizes and statistics). Consistent with our LHb recordings after defeat (Figure 2), we observed a trend of greater LHb activation in susceptible mice ($Z = -1.25$, $p = 0.21$).

To statistically verify this claim of higher cortical activation in resilient mice versus subcortical activation in susceptible mice, we compared the estimated contribution of SI time to Fos^+ cell counts across all Allen CCF brain regions in cortex ($n = 61$ regions) versus subcortical nuclei ($n = 139$ regions). Indeed, cortical regions were significantly more active for high SI time,

compared to subcortical regions ($p \leq 0.001$; Figure 6F).

Next, we performed an analogous analysis of the same data, but instead examining the effect of LHb-stimulation during CSDS versus control stimulation (in YFP mice) on brainwide activation. Consistent with the fact that LHb stimulation produced susceptibility (Figure 5), this revealed a similar pattern between LHb-stimulated versus YFP mice (Figure 6D, bottom) as we had observed in susceptible versus resilient mice (Figure 6D, middle). Compared to controls, LHb-stimulated mice had stronger neural activation in subcortical nuclei and weaker activation in the cortex (Figure 6G), again similar to what we observed for susceptible mice (Figure 6F). This suggests that LHb stimulation produces a similar brainwide pattern of activity to susceptibility.

Further supporting the conclusion that LHb stimulation during defeat produces brainwide substrates of susceptibility, this same pattern of stronger subcortical versus weaker cortical activation in susceptibility was present in a separate “control” cohort that was defeated but that did not receive any LHb stimulation (Figure 6H). Moreover, neural correlates of LHb stimulation and of susceptibility were correlated between these two cohorts across regions (Figure 6I, J).

Taken together, this provides strong evidence that susceptibility is associated with strong subcortical and weak cortical activation, and that LHb stimulation during stress durably shifts activity towards this brainwide substrate of susceptibility.

Discussion

While prior work has uncovered differences between susceptible and resilient mice after CSDS, much less is known about the role of neural teaching signals during stress in driving differences in stress outcomes. Here, we focus on the LHb, which provides a negative teaching signal[32,56–58] and is implicated in aversive learning[33,34] and depression-related behavior[20,34,37–39,59–61], to ask: 1) when and how does activity in the LHb first differ between susceptible and resilient individuals? and 2) do these differences produce behavioral and brainwide correlates of susceptibility?

We found heightened LHb activity during proximal behaviors during and after social defeat (but not before), with little dependence on the specific proximal behavior (Figure 2-3). From the first day of defeat, this elevated activity is stronger in susceptible than resilient mice (Figure 4). LHb stimulation during defeat is sufficient to produce a susceptible phenotype (Figure 5), as well as to generate a persistent shift in the balance of subcortical versus cortical activity that closely resembles the brainwide correlates of susceptibility (Figure 6).

LHb stimulation (and susceptibility) recruits a subcortical network while resilience recruits a cortical network

Stimulation of the LHb during defeat produces sustained, brainwide change in the balance of neural activation of subcortical versus cortical networks (Figure 6). These widespread changes suggest that the progression to resilience versus susceptibility may be mediated in part by a competition over the course of stress between these cortical and subcortical networks, and that LHb activity contributes to controlling this balance.

To our knowledge, this fundamental organization of cortical activation in resilience and

subcortical activation in susceptibility has not previously been demonstrated, despite previous brainwide Fos measurements in similar paradigms[51,62,63]. However, this pattern of changes is consistent with the fact that several cortical regions have been implicated in resilience[63–68] and several subcortical regions have been implicated in susceptibility[23,69–75].

Our ability to make this observation was aided by the high signal to noise and high spatial resolution of our Fos data, the fact that we improved the accuracy of the standard Fos cell detection pipeline by using deep learning, and the visualization of Fos densities across the entire brain between the groups (interactive visualization of data from >3 million detected cells: https://www.brainsharer.org/ng/?id=876).

Separate roles for LHb and VTA dopamine during defeat in the progression to susceptibility versus resilience

LHb neurons inhibit VTA dopamine neurons[35,76–81], and the two populations are thought to have roughly opposite response profiles and functions[32,35]. Consistent with these opposing roles, activation of NAc-projecting DA neurons during defeat biases towards resilience[26], whereas here we show activation of LHb neurons during defeat biases towards susceptibility (Figure 5). Given this, LHb activity during defeat may contribute to susceptibility at least in part by inhibiting pro-resilient VTA DA activity[43].

However, a comparison of the current findings and our previous work[26] points to important differences in the correlates and consequences of activity in LHb versus VTA dopamine neurons during defeat. First, the LHb shows little action selectivity during proximal behaviors during defeat (Figure 3), while NAc-projecting dopamine neurons display clear selectivity to specific actions (e.g. fighting back versus being attacked). Second, differences in activity between susceptible and resilient mice are present from the first day of defeat in LHb (Figure 4), while differences only emerge slowly during defeat in dopamine neurons. Finally, attack-triggered activation of LHb produces susceptibility (Figure 5), while attack-triggered dopamine inhibition does not.

These differences between LHb versus VTA dopamine neurons imply that dopamine neurons are not simply a reflection of LHb activity during defeat, and that LHb-mediated and dopamine-mediated mechanisms of susceptibility versus resilience are at least partially distinct. Since the LHb also sends a major projection to the raphe[82–88], that projection is a good candidate to mediate the effects of LHb activity on susceptibility[59,83,85,89].

One possibility is that LHb activity during defeat primarily controls the progression towards susceptibility (with less control of resilience)[37,39,90], while dopamine activity during defeat primarily controls the progression towards resilience[26,91] (with less control of susceptibility). This is consistent with our inability to produce susceptibility with manipulations of DA neurons during defeat[26] and the broader idea that resilience and susceptibility are distinct and actively learned processes[5,26,92].

If this idea is correct, it could also relate to what causes strengthened subcortical activity in LHb-stimulated (or susceptible) mice, and strengthened cortical activity in unstimulated (or resilient) mice (Figure 6). LHb activity during stress may produce susceptibility by modulating activity in serotonin neurons in the raphe[45,59,83,85] which in turn might lead to the overactive subcortical network in susceptible mice. On the other hand, activity in NAc-projecting DA neurons may cause resilience through strengthened cortical activity (as well as strengthened

NAc activity, which was also present in resilient mice, Extended data table 14). Future work will test these ideas.

Figures

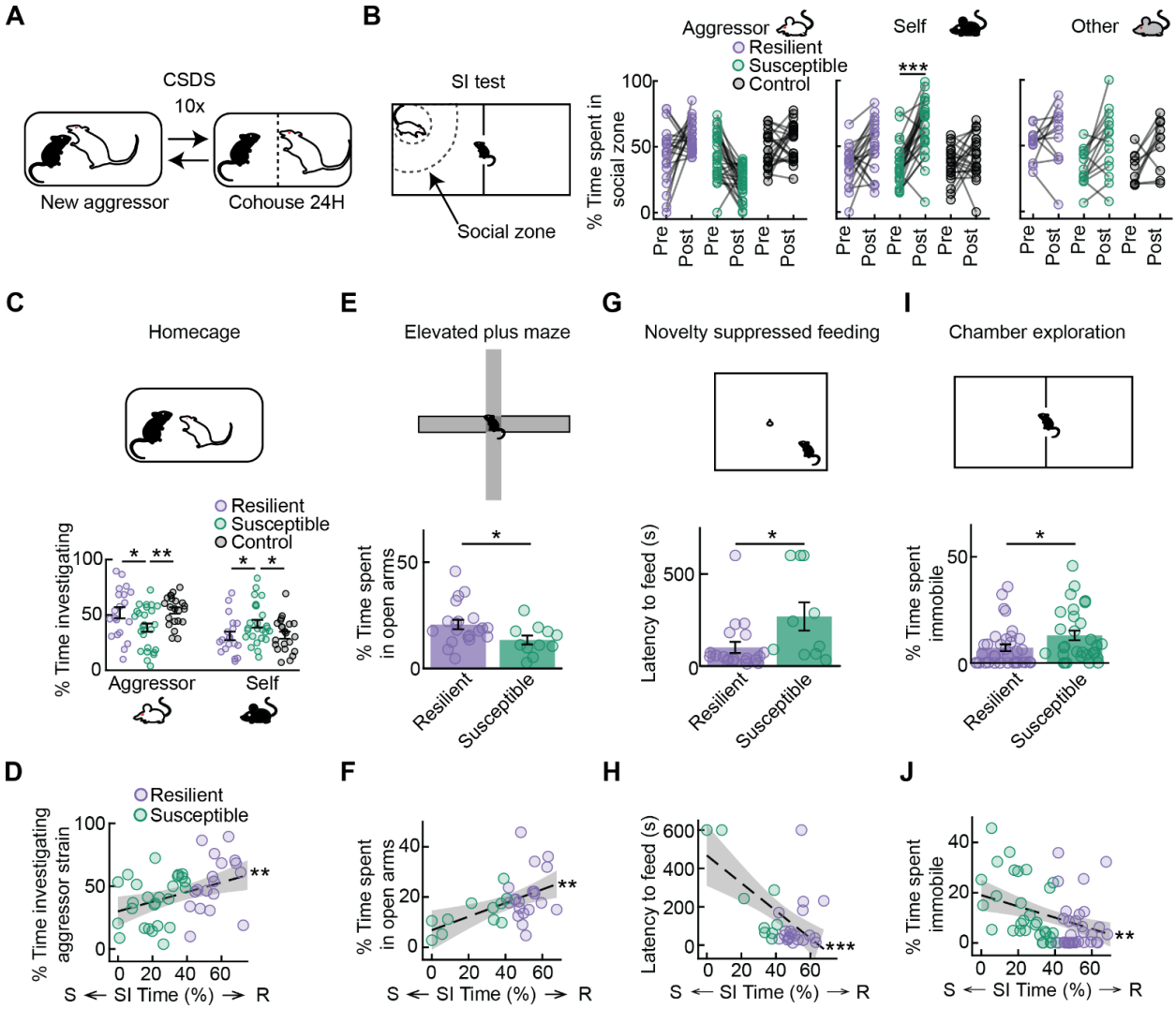

Figure 1. **In susceptible mice, CSDS produced strain-specific aversion and associated changes in anxiety-like behavior and mobility. A**. Schematic of Chronic Social Defeat Stress (CSDS) behavioral paradigm. **B**. Left: schematic of Social Interaction (SI) test. Right: time spent in the social zone (SI time) before vs after CSDS when the social target was of the aggressor (SW), self (BL6) or other (AKR) strain. Self strain susceptible pre-CSDS vs self strain susceptible post-CSDS: t = -6.1047, p <0. 0001. **C**. Top: schematic of homecage assay. Bottom: percent of time spent investigating (sniffing and pursuing) social target in freely-moving assay when the social target was a juvenile of the aggressor strain or a juvenile of the self strain (resilient N = 20, susceptible N = 26, control N = 22). Resilient vs susceptible for aggressor social target: t = -2.1898, p = 0.0339. Susceptible vs control for aggressor social target: t = -3.2324, p = 0.0023. Resilient vs susceptible for self-strain social target: t = 2.0549, p = 0.0460. Susceptible vs control for self-strain social target: t = 2.1285, p = 0.0387. **D.** Relationship between time spent investigating a juvenile from the aggressor strain in the homecage assay and SI time after CSDS: R = 0.3965, p = 0.0064. **E**. Top: Schematic of elevated plus maze (EPM). Bottom: percent of time spent in open arms of EPM (resilient N = 21, susceptible N = 10). Resilient vs susceptible: t = -2.1745, p = 0.038. **F**. Relationship between time spent in open arms of the EPM and SI time: R = 0.5118, p = 0.0032. **G**. Top:

schematic of novelty suppressed feeding assay (NSF). Bottom: Latency to feed during NSF (resilient N = 20, susceptible N = 10). Resilient vs susceptible: t = 2.4426, p = 0.0212. **H**. Relationship between latency to feed in NSF and SI time: R = -0.6323, p = 0.0002. **I**. Top: Schematic of chamber exploration assay. Bottom: Percent of time immobile (speed <1cm/s) during chamber exploration. E. Resilient vs susceptible: t = -2.1302, p = 0.037. **J**. Relationship between time spent immobile during chamber exploration and SI time: R = -0.3757, p =0.0019. p-values in **B** are from a 2-sided t-test (with Bonferroni correction for multiple groups and strains). p-values in **C** are from unpaired 2-sided t-tests following 1-way ANOVA. p-values in **E**, **G**, **I** are from unpaired 2-sided t-tests. p-values in **D**, **F**, **H**, **J** are from Pearson's correlation. Shaded areas in **D**, **F**, **H**, **J** represent 95% confidence interval for linear fit. *$p \leq 0.05$, **$p \leq 0.01$, ***$p \leq 0.001$. See Table 1 for detailed statistics summary.

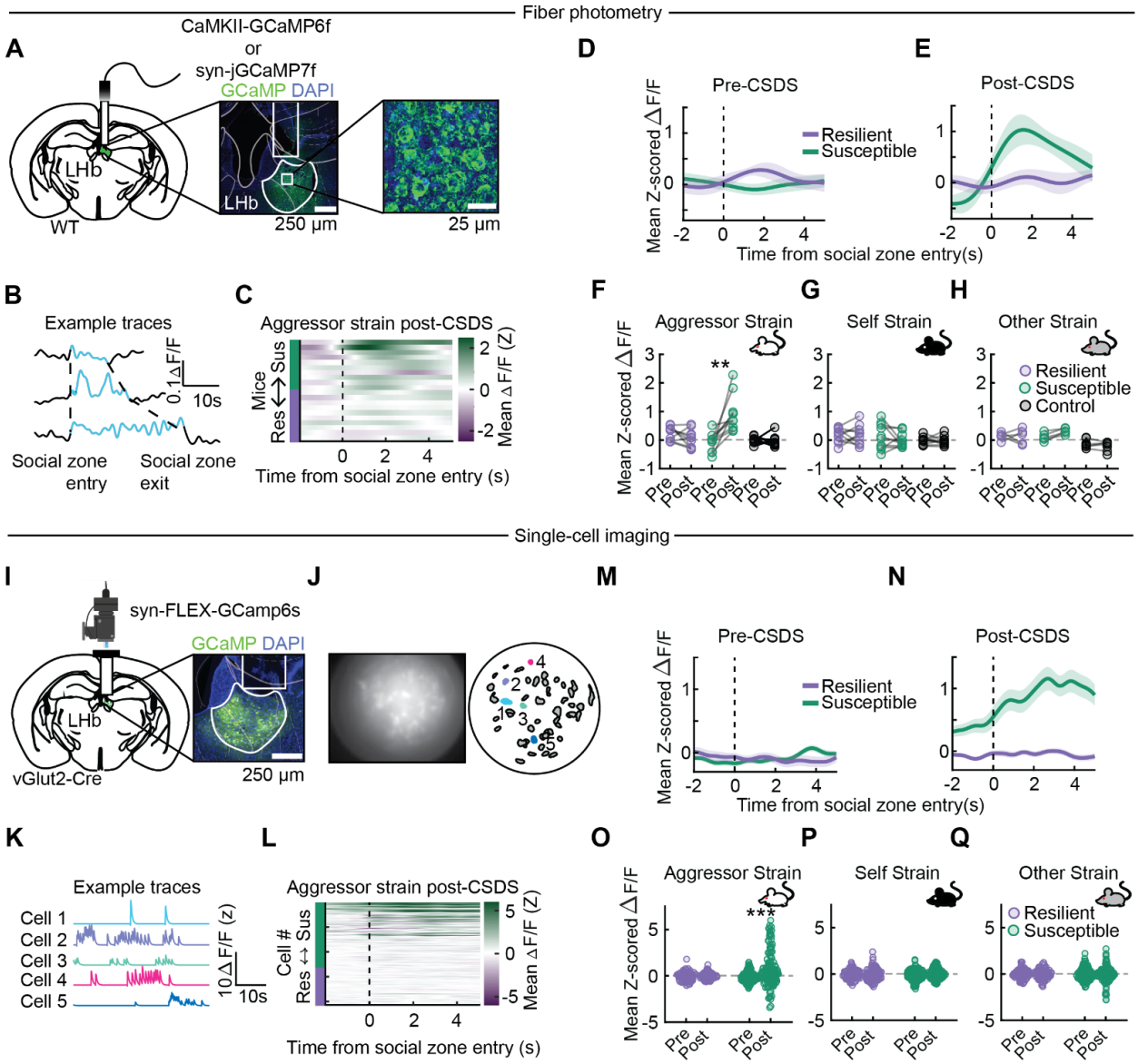

Figure 2. **After but not before CSDS, aggressor strain-specific responses in the LHb of susceptible mice in the SI test. A**. Left: Location of fiber photometry recordings from cell bodies in the Lateral Habenula (LHb) Middle: GCaMP (AAV5-CaMKII-GCaMP6f or AAV5-syn-jGCaMP7f) expression in LHb

cell bodies in green and DAPI in blue. Right: A confocal image of LHb neurons showing nuclear exclusion of GCaMP. **B**. Responses in an example mouse to individual visits to the social zone of the aggressor (Figure 1B). Trials are organized in ascending order of time spent in the social zone . **C**. LHb signal aligned to entry of aggressor social zone during SI test. Each row is mean response in one mouse, with mice sorted by SI time, from susceptible (green, $N = 10$) to resilient (purple, $N = 10$). **D**. LHb signal aligned to entry of aggressor social zone during pre-CSDS SI test, averaged across individuals in resilient and susceptible groups (mean ± s.e.m. plotted). **E**. Same as **D** for LHb signal aligned to entry of aggressor social zone during post-CSDS SI test. **F**. Average of 2s from onset of entry to the social zone in **D** and **E** for susceptible ($N = 10$), resilient ($N = 10$), and control mice ($N = 10$). Susceptible pre-CSDS vs susceptible post-CSDS: $t = -4.1216$, $p = 0078$. **G**. Same as **F** for self-strain social zone entry. **H**. Same as **F** for other strain social zone entry. **I**. Left: Cellular resolution calcium imaging schematic. Right: Example histology with GRIN lens placement above LHb and AAV9-syn-FLEX-GCaMP7f expression in green and DAPI in blue. **J**. Left: Example FOV from microendoscope. Right: Same example FOV, with identified neurons outlined. **K**. Example traces of neurons with filled-in colors in **J**. **L**. LHb signal aligned to entry of aggressor social zone during SI test. Each row is a neuron, sorted from susceptible (green, $N = 131$ neurons, $N = 5$ mice) to resilient (purple, $n = 75$ neurons, $N = 4$ mice). **M**. LHb signal aligned to entry of aggressor social zone during pre-CSDS SI test, averaged across neurons in resilient and susceptible groups (mean ± s.e.m. plotted). **N**. Same as **M**, for LHb signal aligned to entry of aggressor social zone during post-CSDS SI test. **O**. Average of 2s from entry of aggressor social zone in **M** and **N** plotted for susceptible and resilient groups. Susceptible pre-CSDS vs susceptible post-CSDS: $t = -5.7393$, $p < .0001$. **P**. Same as **O** for self-strain social zone entry. **Q**. Same as **O** for other strain social zone entry. *p*-value in **F** is from a paired 2-sided *t*-test (with Bonferroni correction for multiple groups and strains). *p*-value in **O** is from an unpaired 2-sided *t*-test (with Bonferroni correction for multiple groups and strains). See Table 1 for detailed statistics summary.

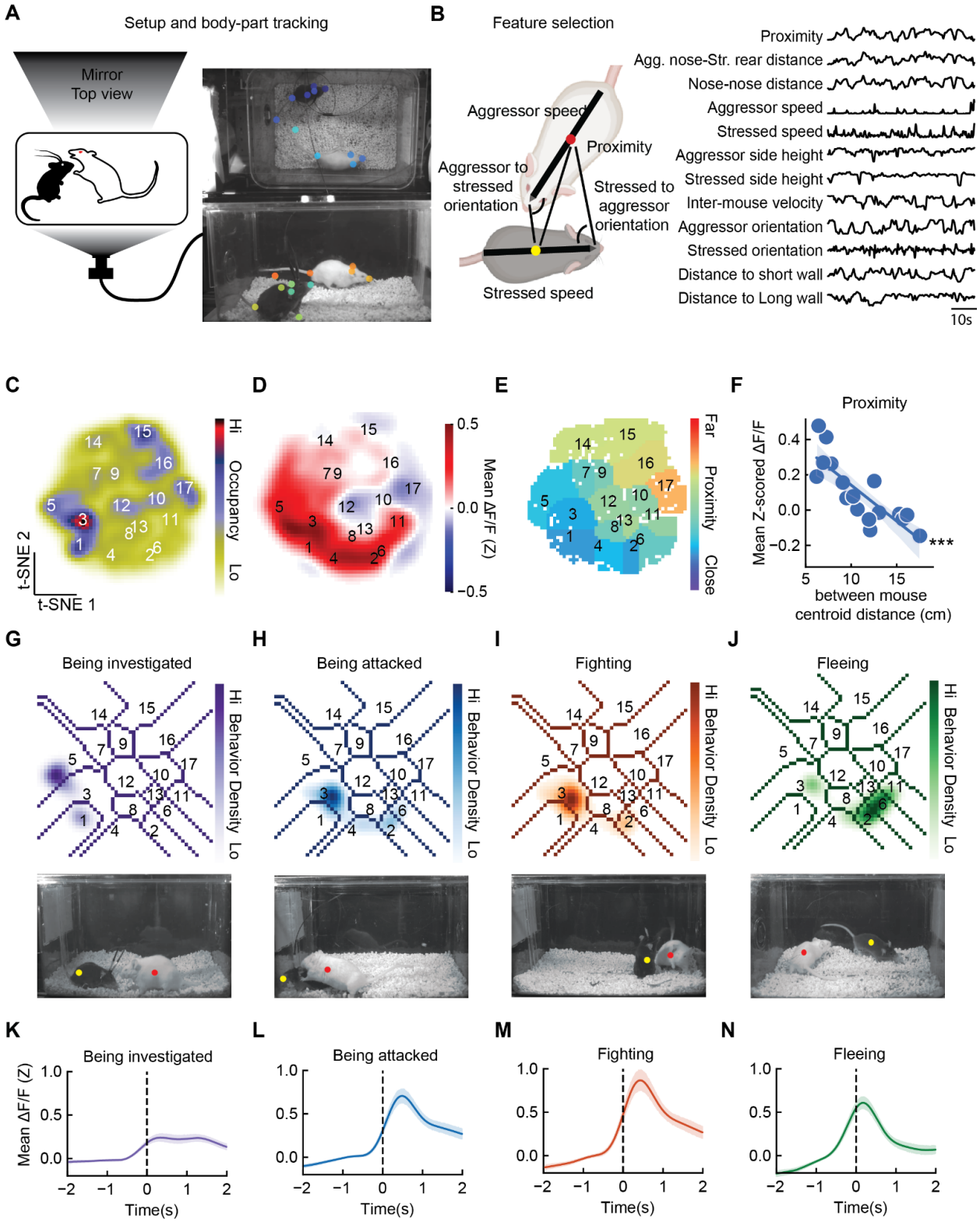

Figure 3. During CSDS, elevated LHb activity during attack and other proximal behaviors. A. Left: Behavioral setup. Right: Example video frame with tracked key points. **B**. Left: Features calculated from key points. Right: Time series of all features used in behavior quantification. **C**. Smoothed histogram of *t*-SNE embeddings from features, with clusters numbered by increasing distance between mice. **D**. Mean

LHb GCaMP signal across *t*-SNE behavior space in fiber photometry mice. **E**. Average proximity within each *t*-SNE cluster. **F**. For each cluster, mean LHb GCaMP signal plotted against mean centroid distance between mice (R = -0.8210, p = 5.4E-5, N = 17 clusters). **G**. Top: Density of random forest classified investigation within *t*-SNE space. Bottom: Example frame of being investigated. Stressed mouse: yellow dot; aggressor mouse: red dot. **H**. Top: Density of random forest classified attack within *t*-SNE space. Bottom: Example frame of attack. Stressed mouse: yellow dot; aggressor mouse: red dot. **I**. Density of random forest classified fighting within *t*-SNE space. Bottom: Example frame of fighting. Stressed mouse: yellow dot; aggressor mouse: red dot. **J**. Density of random forest classified fleeing within *t*-SNE space. Bottom: Example frame of fleeing. Stressed mouse: yellow dot; aggressor mouse: red dot. **K**. Neural activity in LHb time-locked to being investigated (mean ± s.e.m. plotted). **L**. Neural activity in LHb time-locked to being attacked (mean ± s.e.m. plotted). **M**. Neural activity in LHb time-locked to fighting (mean ± s.e.m. plotted). **N**. Neural activity in LHb time-locked to fleeing (mean ± s.e.m. plotted). *p*-value in **F** is from Pearson's correlation. Shaded areas in **F** represent 95% confidence interval for linear fit. $^{*}p \leq 0.05$, $^{**}p \leq 0.01$, $^{***}p \leq 0.001$. See Table 1 for detailed statistics summary. See Table 1 for detailed statistics summary.

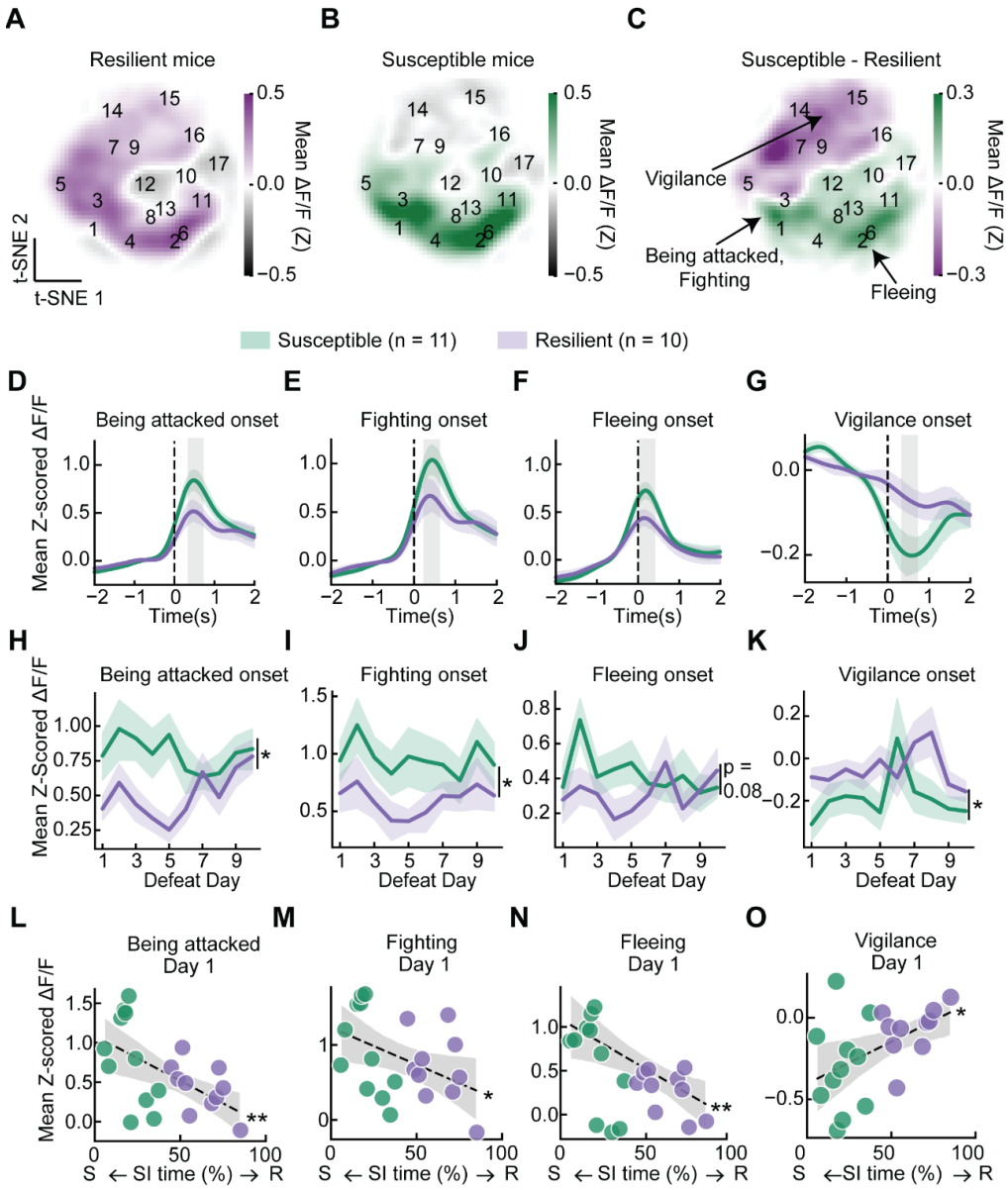

Figure 4. From the 1st day of defeat, higher LHb activity in susceptible mice during proximal behaviors and in resilient mice when vigilant. A. Mean LHb GCaMP dF/F across *t*-SNE behavior space in susceptible mice (across all 10 days of defeat; N=11). **B**. Mean LHb GCaMP dF/F across *t*-SNE behavior space in resilient mice (across all 10 days of defeat; N=10). **C**. Difference between susceptible and resilient LHb GCaMP dF/F (difference between panel **A** and **B**). **D**. Being attacked onset-aligned LHb responses during defeat averaged across individuals in resilient and susceptible groups (mean ± s.e.m. plotted). Grey region indicates +/-0.2s surrounding the peak response. **E**. Fighting back onset-aligned LHb dF/F during defeat. Grey region indicates +/-0.2s surrounding the peak response. **F**. Fleeing onset-aligned LHb dF/F during defeat. Grey region indicates +/-0.2s surrounding the peak response. **G**. Vigilance onset-aligned LHb DF/F during defeat. Grey region indicates +/-0.2s surrounding the minimum response. **H**. Average LHb GCaMP dF/F to attack onset from resilient and susceptible groups across defeat (mean ± s.e.m across mice; averaging across labeled gray region (+/-0.2s peak response) in **D**). Onset activity by SI time, day, and their interaction: main effect of SI time, $Z = -2.529$, $p = 0.011$; main effect of day, $Z = 0.483$, $p = 0.629$. Interaction, $Z = 2.066$, $p = 0.039$. **I**. Average LHb GCaMP dF/F to fighting onset from resilient and susceptible groups across defeat (mean ± s.e.m across mice; averaging across labeled gray region (+/-0.2s peak response) in **E**). Onset activity by SI time, day, and their

interaction: main effect of SI time, $Z = -2.063$, $p = 0.039$; main effect of day, $Z = -0.446$, $p = 0.655$. Interaction, $Z = 0.840$, $p = 0.401$. **J**. Average LHb GCaMP dF/F to fleeing onset from resilient and susceptible groups across defeat (mean ± s.e.m across mice; averaging across labeled gray region (+/-0.2s peak response) in **F**). Onset activity by SI time, day, and their interaction: main effect of SI time, $Z = -1.738$, $p = 0.082$; main effect of day, $Z = -0.496$, $p = 0.620$. Interaction, $Z = 2.551$, $p = 0.011$. **K.** Average LHb GCaMP dF/F to vigilance onset from resilient and susceptible groups across defeat (mean ± s.e.m across mice; averaging across labeled gray region (+/-0.2s minimum response) in **G**). Onset activity by SI time, day, and their interaction: main effect of SI time, $Z = 2.1441$, $p = 0.032$; main effect of day, $Z = 0.720$, $p = 0.471$. Interaction, $Z = 0.313$, $p = 0.754$. **L**. Average LHb GCaMP responses to attack onset (labeled gray region in **D**) on day 1 plotted against SI time for each mouse ($N = 21$ mice): $R = -0.5571$, $p = 0.0087$. **M**. Average LHb GCaMP responses to fighting onset (labeled gray region in **E**) on day 1 plotted against SI time for each mouse ($N = 21$ mice): $R = -0.4374$, $p = 0.0474$. **N**. Average LHb GCaMP responses to fleeing onset (labeled gray region in **F**) on day 1 plotted against SI time for each mouse ($N = 21$ mice): $R = -0.5580$, $p = 0.0086$. **O**. Average LHb GCaMP responses to vigilance onset (labeled gray region in **G**) on day 1 plotted against SI time for each mouse ($N = 21$ mice): $R = 0.4931$, $p = 0.0231$. *p*-values in **H**-**K** are from two-sided GEE. *p*-values in **L-O** are from Pearson's correlation. Shaded areas in **L**-**O** represent 95% confidence interval for linear fit. *$p \leq 0.05$, **$p \leq 0.01$, ***$p \leq 0.001$. See Table 1 for detailed statistics summary. See Tables 2-9 for more information on GEE statistics.

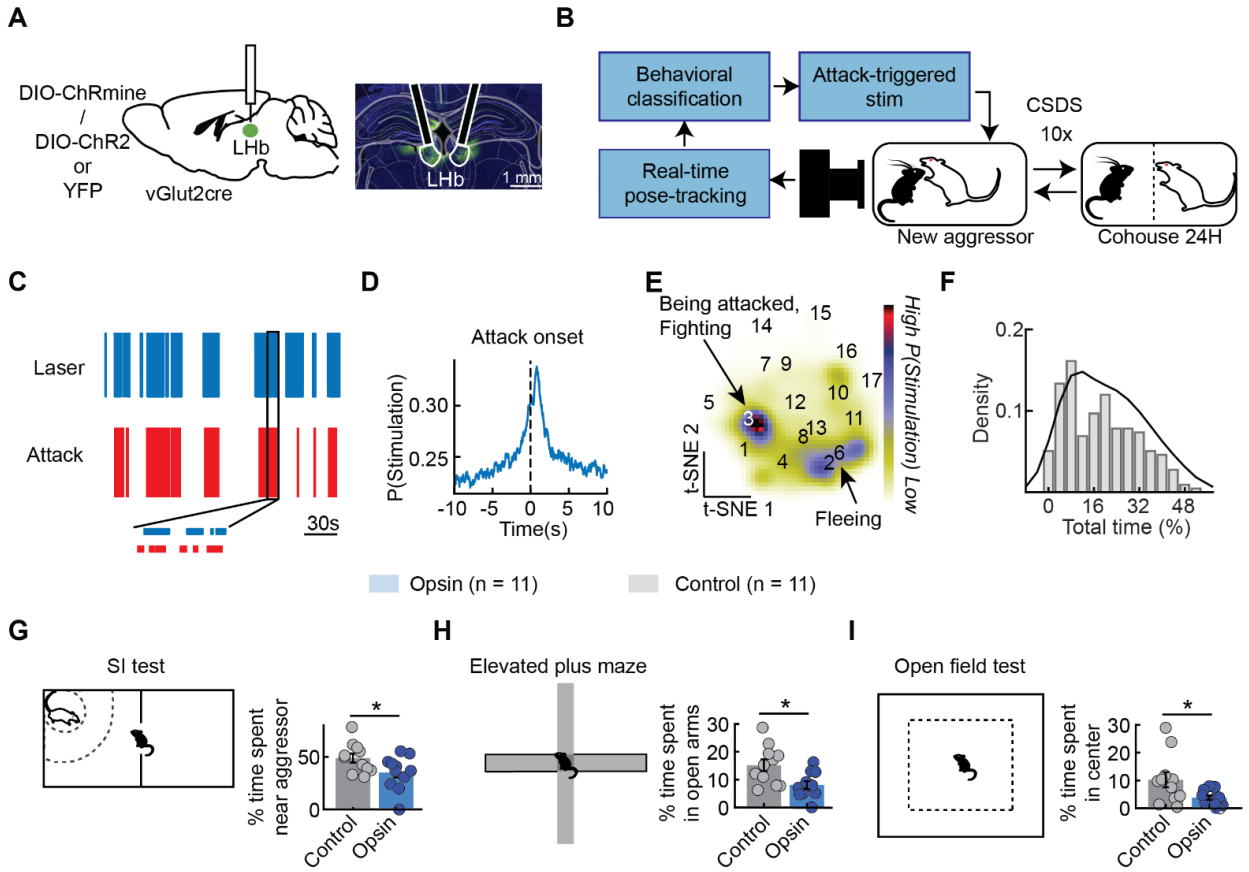

Figure 5. Closed-loop LHb stimulation during CSDS produces susceptibility. A. Left: Location of virus injections and fiber targeting of cell bodies in the Lateral Habenula (LHb). Right: Example histology of virus expression. **B**. Schematic of attack-triggered stimulation. Each detected attack frame during defeat triggered 5 pulses of 20 Hz stimulation. **C**. Example of a defeat session with laser light delivery triggered on attack of the closed-loop mouse. Bottom inset is a 10s segment. **D**. Probability of a laser train, as a function of time relative to attack onset. **E**. Density of stimulation in *t*-SNE space. **F**. Distribution across sessions of percent of defeat session that mice received laser (mean is 21.34% of the defeat session). **G**. Difference in SI time between opsin and control group. Opsin vs control: $t = -2.1263$, $p = 0.0461$. **H**. Difference in open-arm time in the elevated plus maze between opsin and control group. Opsin vs control $t = -2.2934$, $p = 0.0328$. **I**. Difference in center time in the open field between opsin and control group. Opsin vs control $t = -2.8231$, $p = 0.0105$. *p*-values in **G**-**I** are from unpaired 2-sided *t*-tests. $^*p \leq 0.05$, $^{**}p \leq 0.01$, $^{***}p \leq 0.001$. See Table 1 for detailed statistics summary.

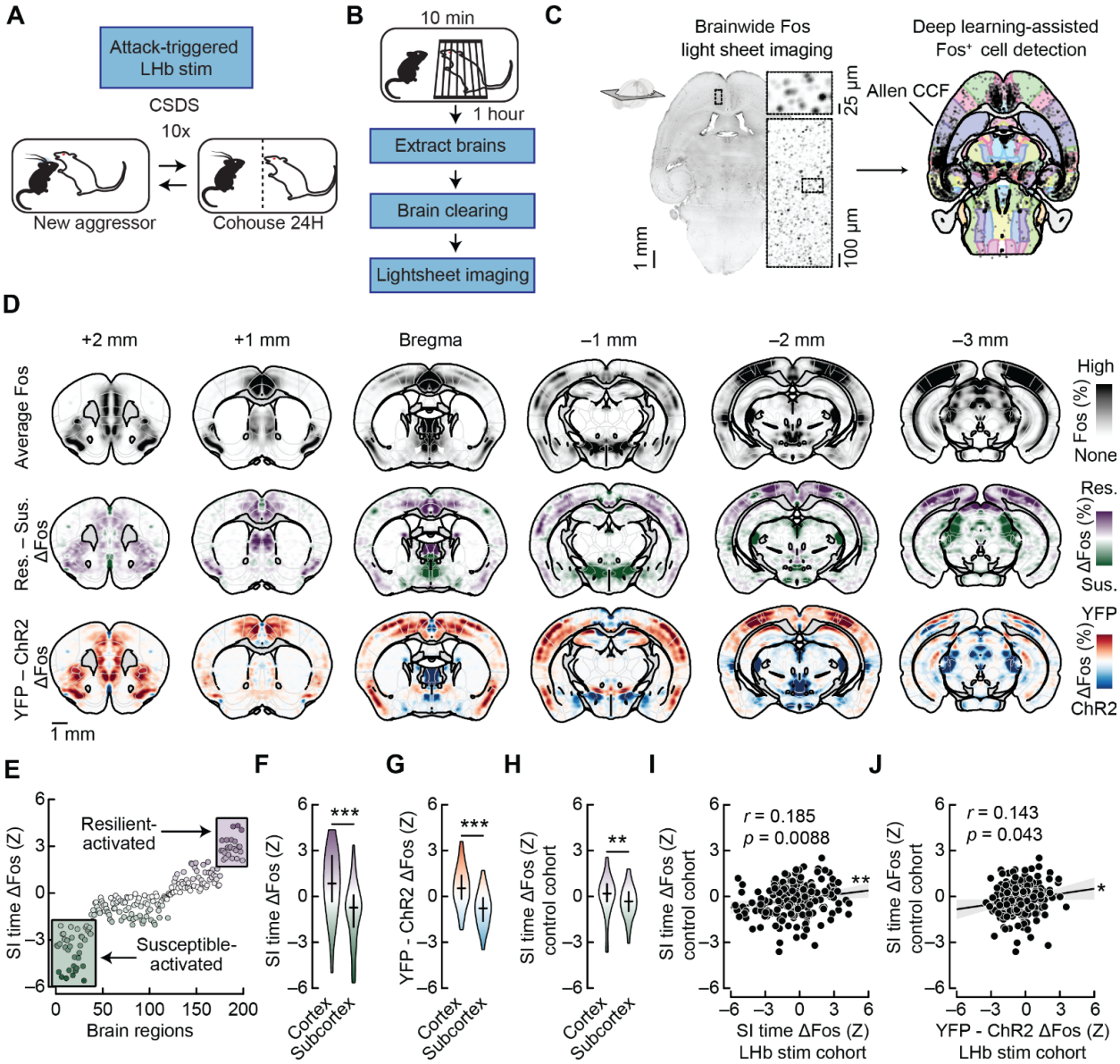

Figure 6. LHb stimulation during CSDS (and susceptibility) durably recruits a subcortical network while resilience recruits a cortical network. A. Schematic of attack-triggered stimulation. **B**. Approximately one week after the conclusion of CSDS, brains were extracted, followed by clearing and imaging. **C**. Left: example brainwide Fos imaging data. A 50-plane (100-µm) maximum intensity projection is shown. The insets are shown after background subtraction and filtering. Right: All detected cells overlaid on the Allen CCF for the example section on the left. **D**. Total estimated density of Fos$^+$ cells across all mice (top row; N = 15 mice; n = 3,246,281 total cells), the difference in estimated density across resilient (N = 7) and susceptible (N = 8) mice (middle row), or the difference in estimated density across ChR (N = 10) and YFP (N = 5) mice (bottom row). **E**. Individual Allen CCF brain regions sorted by the estimated contribution of SI time to Fos$^+$ cell counts based on GLM coefficients (N = 15 mice). Regions that were significantly different are highlighted with purple (resilient-activated) and green (susceptible-activated) boxes. Significance is based on GLM coefficient estimate z-tests corrected for 10% false discovery rate. **F**. Distribution of estimated SI time contribution to Fos$^+$ cell counts across all Allen CCFv3 brain regions in cortex (n = 61 regions) and subcortical nulei (n = 139 regions). Cortex vs. subcortical nuclei: ks = 0.448, p = 4.0E-8. **G**. Distribution of estimated ChR2 contribution to Fos$^+$ cell counts across all Allen CCFv3 brain regions in cortex (n = 61 regions) and subcortical nucleix (n = 139

regions). Cortex vs. subcortical nuclei: *ks* = 0.472, *p* = 5.8E-9. **H**. Distribution of estimated SI time contribution to Fos^+ cell counts across all Allen CCFv3 brain regions in cortex (*n* = 61 regions) and subcortical nuclei (*n* = 139 regions) for the control cohort. Cortex vs. subcortical nuclei: *ks* = 0.282, *p* = 0.0018. **I.** Correlation between the estimated SI time contributions to Fos^+ cell counts for the control cohort vs the LHb stimulation cohort (*n* = 200 regions): *r* = 0.185, *p* = 0.0088. **J**. Correlation between the estimated SI time contributions to Fos^+ cell counts for the control cohort vs the estimated ChR2 contributions to Fos^+ cell counts (*n* = 200 regions): *r* = 0.143, *p* = 0.043. Error bars in **F**-**H** represent interquartile range. Shaded areas in **I**, **J** represent 95% confidence interval for linear fit. *p*-values in **F**-**H** are from Kolmogorov-Smirnov tests. *p*-values in **I**, **J** are from Pearson's correlation. *$p \leq 0.05$, **$p \leq 0.01$, ***$p \leq 0.001$. See Tables 1, 14-15 for detailed statistics summary.

Methods

Mice. All experiments were approved by the Princeton University Institutional Animal Care and Use Committee and were in accordance with National Institutes of Health standards. Prior to and throughout experimental assays, experimental and stimulus animals were housed under a 12 H light-dark cycle with experiments exclusively taking place during the dark phase. Mice used in this study were C57BL/6J males (Jackson Laboratory Strain #000664) between the ages of 8 and 24 weeks old, Swiss Webster males (Taconic Farms #Tac:SW) between the ages of 8 and 57 weeks, and AKR/J males (Jackson Laboratory Strain #000648) between the ages of 8 and 16 weeks old. A total of 114 mice were used for recordings and manipulation: 57 for fiber photometry, 11 for cellular resolution calcium imaging, and 22 for optogenetics experiments. An additional 141 mice were used as stimulus mice (social targets or aggressors): 90 Swiss Websters, 33 C57BL6/J, and 18 AKR/J. Mice undergoing fiber photometry experiments and mice undergoing Fos experiments were wild-type. Mice undergoing cellular resolution calcium imaging experiments and mice undergoing optogenetic experiments were vGlut2-cre (Jackson Laboratory strain #016963). Food and water were given *ad libitum*.

Surgery. At 4-12 weeks of age, animals were anesthetized (isoflurane at 5% for induction and 1-2% for maintenance) and leveled with a stereotaxic frame before injections and implants were done.

For fiber photometry recordings, mice were injected with 80 nL of viral vector expressing a GCaMP (cohort 1: AAV5-CaMKII-GCaMP6f-WPRE-SV40 at a titre of 3.13E13 genome copies/mL produced by addgene or cohort 2: AAV5-syn-jGCaMP7f-WPRE-SV40pA at a titre of 2.5E14 genome copies/mL produced by PNI viral core) in the LHb (AP -1.6 mm, ML +/- 0.46 mm, DV -3 mm relative to the skull surface at Bregma) and implanted with 400 µm core diameter optical fibers (MFC_400/430-0.48_4mm_MF2.5_FLT from Doric Lenses Inc.) in the LHb (AP -1.6 mm, ML +/- 0.46 mm, DV -2.4 mm relative to the skull surface at Bregma), with hemisphere selection counterbalanced between animals. Metabond (Parkell) was used to fix fibers to the skull. Ortho-Jet Crystal mixed with carbon glassy, spherical powder (Sigma-Aldrich) was then used to further secure the implants to the metabond. Mice were allowed to recover for at least a week before starting CSDS.

For cellular resolution calcium imaging experiments, mice were injected with 80 nL of viral vector expressing a GCaMP (AAV9-syn-FLEX-GCamp6s-WPRE at a titre of 2.13E13 genome copies/mL produced by addgene). At least 5 days later, animals were implanted with a 0.5mm diameter GRIN lens (1050-004610, Inscopix) in the LHb (AP -1.6 mm, ML +/- 0.47 mm, DV -2.45 mm relative to the skull surface at Bregma). At least 4 weeks later, a baseplate (1050-004638, Inscopix), attached to the miniature microscope (nVISTA 3.0, Inscopix), was positioned over the GRIN lens such that the neurons were in focus. The baseplate along with a titanium headplate[93] were then secured to the skull using Ortho-Jet Crystal mixed with carbon glassy, spherical powder (Sigma-Aldrich), and a baseplate cover (1050-004639, Inscopix) was used to protect the GRIN lens.

For optogenetic experiments, vGlut2-cre animals were injected with 60 nL of viral vector expressing ChR2 (AAV5-EF1a-DIO-ChR2-eYFP) at a titre of 2.40E+13 or 80 nL of viral vector expressing ChRmine (AAV5-EF1a-DIO-ChRmine-EYFP/mScarlet-WPRE-HGHpA at a titre of 1.8E13 genome copies/mLproduced by the PNI virus core) or YFP (AAV5-EF1a-DIO-EYFP-WPRE-hGHpA at a titre of 1.5-2E14 genome copies/mL produced by the PNI virus core) in the LHb (AP -1.6 mm, ML +/- 0.46 mm, DV -3 mm relative to the skull

surface at Bregma) and implanted bilaterally with a 200 µm core diameter optical fibers above the LHb (AP -1.6 mm, ML +/- 0.87 mm, DV -2.28 mm relative to the skull surface at Bregma, inserted at a 10º angle). Mice were allowed to express virus for a minimum of 4 weeks before behavioral experiments were initiated.

Fiber photometry data acquisition. GCaMP fiber photometry recordings were collected through two different systems. Data from cohort 1 was collected using a fiber photometry set-up similar to that described in Gunaydin et al., 2014. A 488 nm laser light (Micron Technology) was filtered (FL488, Thor Labs), passed through a dichroic mirror (MD498, Thor Labs), and delivered through a patch cable (MFP_400/430/1100-0.48_2m_FCM-MF2.5, Doric Lenses) which was coupled to the fiber attached to the mouse via a ceramic split sleeve (2.5 mm diameter, Precision Fiber Products). The laser, which was modulated at 210.999 Hz, was controlled by a lock-in amplifier (Ametek, 7265 Dual Phase DSP Lock-in Amplifier). Fluorescent emission from GCaMP6f at 500-550 nm then passed through the same patch cable and dichroic mirror into a photodetector (Model 2151, New Focus), and the signal was filtered at the same 210.999 Hz using the same lock-in amplifier, and a time constant of 20 ms. AC gain on the lock-in amplifier was set to 0 dB. The signal was digitized at 1000 Hz.

Data from cohort 2 was collected using a set-up similar to that described in Willmore et al., 2022. We used a Doric Lenses photometry system (4-channel driver LEDD_r, LEDs at 465 (and 405 nm in a subset of animals), fluorescence mini cube FMC5_E1(465-480)_F1(500-540)_E2(555-570)_F2(580-680)_S, and Newport Visible Femtowatt Photoreceiver Module NPM_2151_FOA_FC). The system was driven by and recorded from using custom code written for a real-time processor (RZ5P, Tucker Davis Technologies) in OpenWorkBench (v.2.28.0). GCaMP was excited by driving a 465 nm light-emitting diode (LED) light (about 400 Hz sinusoidal modulation, at an intensity of around 10 µW, filtered between 465 and 480 nm) delivered to the brain through a fiber optic patch cord (MFP_400/430/1100-0.48_2m_FCM-MF2.5). The emission fluorescence passed from the brain through the same patch cords and was filtered (500–520 nm), amplified, detected, and demodulated in real-time by the system. Demodulated fluorescence signals were saved at a rate of about 1 kHz. Modulation at the 405 nm wavelength was not used for processing GCaMP signals.

Inscopix data acquisition. Data were acquired with nVista 3.0 using Inscopix Data Acquisition Software v1.7.1 (Inscopix) at 25 FPS, LED power at 0.3 mW/mm^2. To synchronize imaging data with behavior, we recorded TTL sync pulses from the microscope and TTLs from the waveform generator (pulse pal) used to control video frame acquisitions.

Histology in brain slices. Mice were injected with euthasol and perfused with 4% PFA dissolved in 1x PBS. Brains were extracted and post-fixed in 4% PFA for 12–24 H, after which they were cryoprotected in 30% sucrose. Cryosections of the frozen tissue (40 µm slices) were made and stamped directly onto glass microscope slides. Slices were washed with PBS or, for immunohistochemistry, PBS+0.4% Triton (PBST). Then, for immunostaining, a blocking buffer (PBST with 2% normal donkey serum and 1% BSA) was applied for 30 min, followed by incubation by a primary antibody at 4 °C for 12–24 H. Following primary antibody incubation, slides were washed with PBST (5 rounds of 10 min each) followed by incubation at room temperature in a secondary antibody for 2 H, and a final set of washes in PBS (5 rounds of 10 min each). Stained or unstained slides were then dried and coverslipped with a mounting medium (EMS Immuno Mount DAPI and DABSCO, Electron Microscopy Sciences, 17989-98, lot 180418). After at least 12 H of drying, slides were imaged with a digital robotic slide scanner (NanoZoomer S60, C13210-01, Hamamatsu). The following antibodies were used: rabbit anti-GFP (Novus Biologicals CAT# NB600-308) 1:500, Donkey anti-Rabbit Alexa 647

(ThermoFisher Scientific CAT# A-31573), 1:1000.

Behavior

Video recordings. For the chronic social defeat stress and homecage assays (described below), we used a BlackFly S camera (FLIR, BFS-U3-32S4M-C: 3.2 MP, 118 FPS, Sony IMX252, Mono) and recorded videos with Motif software (Loopbio). The camera was triggered by a Pulse Pal v2 (Sanworks, #1102) at a rate of 100 frames per second (FPS). The camera was oriented at 90° towards the side of the preparation and also captured the top-down view of the preparation with a mirror mounted at a 40° angle above the horizontal.

For all other behavioral assays, recordings were performed using an analog camera and Ethovision (Noldus) software which was used to track the mice.

Chronic social defeat stress (CSDS). Mice were placed in the cage of a novel aggressor for 5 min of free interaction. Afterward a perforated acrylic barrier (Tap Plastics) was placed between the mice. 24H later, mice were placed in the cage of a new aggressor. This continued for a total of 10 days. Unstressed controls were pair-housed with a perforated barrier separating the two mice. They were handled and their cages rotated each day for 10 days. Following the defeat on day 10, aggressors were removed and all mice were singly housed in the shoebox cages through the remaining stages of the experiment.

Defeated mice were housed in the shoebox home cages (#5 Expanded Mouse Cage 22.2 x 30.8 x 16.2 cm, Thoren Caging Systems, Inc.). For recordings, food was removed from the cage and the typical stainless steel lids were replaced with a custom-cut sheet of clear acrylic (Tap Plastics) with a hole for patch cables to run through. Shoebox cages were placed underneath the angled mirror and video recordings were made as described above.

Social interaction test. Mice were placed in a two-chamber arena (56 cm x 24 cm) for 5 minutes with two empty mesh pencil cups in the far left and right corners. The mouse was then removed from the chamber, and a novel social target was placed beneath one cup. The mouse was then returned to the recording chamber for an additional 5 minutes. Mouse location was tracked via Ethovision (Noldus). We quantified the time spent within the social zone (up to 6.5 cm from the enclosure). Following day 10 of defeat, the time spent in the social interaction zone when the social target was a novel swiss webster aggressor was used to delineate resilient and susceptible mice. We defined susceptible as 1 standard deviation below the mean social interaction time of the unstressed control group[26].

Elevated plus maze. Following CSDS, mice were placed in the center of an elevated plus maze (2 enclosed arms and 2 open arms; each arm 76 cm long and 6.5 cm wide). The mouse explored the maze for 7 minutes, while its centroid location was tracked via Ethovision (Noldus). The time spent in the open arms and center of the maze was measured.

Open field test. Mice were placed into the center of an empty area (50 cm x 50 cm). Lamps were used to illuminate the arena on the left and right so that there was a shaded area along the left and right walls. The center was 42 cm x 42 cm centered at the center of the arena. The animal explored for 10 minutes, while its centroid location was tracked via Ethovision (Noldus). The time spent in the center was measured.

2-chamber exploration. Animals were placed in a two-chamber arena (56 cm x 24 cm) for 5 minutes. Mouse location and speed were continuously tracked via Ethovision (Noldus). We quantified the amount of time spent immobile (speed < 1cm/s).

Novelty-suppressed feeding. Mice were placed in the corner of a brightly lit, novel chamber (25 x 25 cm) with a single yogurt chip placed in the center of the camber on a plastic platform. The latency to initiate consumption of the treat was scored. After the first consumption bout, mice were placed back in their home cages with *ad libitum* food access. Mice were food deprived for 18H.

Homecage assay. After defeat, video and neural recordings were taken as mice freely interacted with novel juvenile male C57BL6/J or Swiss Webster social targets. Recordings took place on the same setup described above for recording defeat. Behavior occurred in clean shoebox cages of the same type that was used for defeat. After at least 1 minute of baseline recording mice were presented with the novel mouse. Video (100 FPS) and neural recordings were taken for an additional 9 minutes. Sniffing and pursuit of the social target were then hand-scored.

Behavioral schedule for each cohort. Animals undergoing fiber photometry recordings were subject to the following assays in this order: social interaction assay (with a Swiss Webster, C57BL6/J, and then AKR/J social target in that order on different days), chronic social defeat stress (10 days), social interaction assay (with a Swiss Webster, C57BL6/J and then AKR/J social target in that order on different days), and homecage assay (C57BL6/J and then Swiss Webster social target, or vice versa, randomly assigned on different days). Altogether there were two cohorts of fiber photometry recordings. Animals undergoing cellular resolution calcium imaging were subject to the following assays in this order: social interaction assay (with a Swiss Webster, C57BL6/J, and then AKR/J social target in that order on different days), chronic social defeat stress, social interaction assay (with a Swiss Webster, C57BL6/J and then AKR/J social target in that order on different days), elevated plus maze assay, novelty suppressed feeding assay, open field test, and homecage assay (C57BL6/J and then Swiss Webster social target, or vice versa, randomly assigned on different days). Animals undergoing optogenetic or Fos experiments were subject to the following assays in order: chronic social defeat stress, social interaction assay with a Swiss Webster, elevated plus maze assay, open field test, and novelty suppressed feeding assay. Mice undergoing optogenetic and Fos experiments were also placed for 10 min into the cage of a novel Swiss Webster aggressor that was retrained under a wire cup prior to being sacrificed an hour later for Fos analysis.

Closed-loop, behavior-triggered activation during defeat. To deliver closed-loop attack-triggered optogenetic stimulation (Figure 5), we used a pre-trained random forest (described above) for inference on video frames streamed in real-time.
Images were acquired using a FLIR BlackFlyS camera connected directly to our behavior inference computer (Ubuntu 18.04.06, equipped with a Nvidia GeForce GTX 1070 Ti graphics card). Using publicly available custom code, each video frame was captured by Motif (Loopbio) software and sent as an input to our pre-trained DeepLabCut network for estimating the positions of the interacting mice. The 12 features we defined above were calculated with minor modifications (no smoothing, using adjacent frames for instantaneous speed and velocity features). We trained a separate binary random forest classifier to detect attack behavior from the unsmoothed features using the same training set as mentioned above for the offline analysis. After detection of an attack video frame, a serial signal was passed through the USB to an Arduino, which translated the signal into a TTL for triggering the laser light delivery protocol. The frame capture, behavior inference, and trigger delivery code were run in an open loop and could achieve a speed of about 20 FPS. A list of time stamps from each frame and its probability of behavior detection and whether a trigger was delivered were saved for synchronization.

Blue (447 nm, 5 mW for ChR2 animals) or green (532 nm, 0.8 mW for ChRmine animals) lasers were connected to a commutator (Doric Lenses, FRJ_1x2i_FC-2FC_0.22), which led to 200-μm diameter patch cords that were fastened to the implants of mice through plastic sleeves surrounded by black electric tape. When an attack frame was detected, phasic stimulation was delivered (5 pulses of 5 ms in duration at 20 Hz). Once an attack frame was detected, laser stimulation could not be triggered until all 5 pulses had occurred. Pulses were continuous so long as attack behavior was ongoing. Laser stimulation pulses were recorded for synchronization. Stimulation was performed across all 10 days of defeat, but not during post hoc testing.

Behavioral analysis

Behavioral Annotation. Ground truth for supervised classification of behaviors during defeat (Figure 3-5) was determined by hand annotations of videos scored with BORIS[94]. The following behaviors were annotated: mouse being attacked, mouse being sniffed, mouse fighting back, stressed mouse running away, and mice being vigilant.

Marklerless pose tracking. For fiber photometry and optogenetics experiments, DeepLabCut[95] was used for tracking the positions of the stressed and aggressor mice during defeat. The training set included 1603 frames from 350 videos across 35 mice from 2 separate defeat cohorts). The following points were tracked:

- TopStressNose
- TopStressRightEar
- TopStressLeftEar
- TopStressFiberBase
- TopStressTTI
- TopStressTTip
- TopAggNose
- TopAggRightEar
- TopAggLeftEar
- TopAggTTI
- TopAggTTip
- BottomStressNose
- BottomStressRightEar
- BottomStressLeftEar
- BottomStressFiberBase
- BottomStressRightForePaw
- BottomStressLeftForePaw
- BottomStressTTI
- BottomStressTTip
- BottomAggNose
- BottomAggRightEar
- BottomAggLeftEar
- BottomAggTTI
- BottomAggTTip
- TopDividerRight
- TopDividerLeft
- BottomDividerTopRight
- BottomDividerTopLeft

(TTip: Tail tip, TTI: Tail-torso interface, Stress: stressed mouse, Agg: aggressor) DLC training was run for 1.03 million iterations with default parameters: training frames selected by kmeans clustering of each video session in the training set, trained on 95% of labeled frames, initialized with ResNet-50, batch size of 4.

Feature definition. To define the defeated mouse's posture with respect to his environment and the aggressor, we converted pose data to the following behavioral features:

1. Between centroid distance: Euclidean distance between the midpoint between each mouse's tail-body interface and nose, defined by the top-down view.
2. Distance between aggressor nose and stressed mouse rear
3. Distance between aggressor nose and stressed mouse nose
4. Between centroid velocity: instantaneous (every 8 frames or 0.08s) change in between centroid distance, median smoothed with a window of 0.17 s.
5. Aggressor speed: instantaneous distance between centroid position every 10 frames, smoothed as above
6. Stressed mouse speed: same as above
7. Orientation of aggressor with respect to stressed mouse
8. Orientation of stressed mouse with respect to the aggressor
9. Height of the aggressor: side view nose Y position
10. Height of stressed mouse: same as above
11. Distance of stressed mouse from the closest short wall of the cage: based on top-down view
12. Distance of the stressed mouse from the closest long wall of the cage

Feature preprocessing. Before using features for random forest classification or unsupervised behavior classification, features were preprocessed. Features were truncated to fall within the 1st and 99th percentile of all recorded data for each feature (to remove extreme outliers), smoothed across time with a Gaussian filter of 0.20 s, and rescaled from −1 to 1 (sklearn.preprocessing.MixMaxScaler) within each session to account for variability in mouse size and slightly varying camera angle or height. We chose to rescale features so that no single feature dominates owing to higher magnitude while maintaining the original feature distributions and their covariances, properties that would not be maintained if each feature were normalized independently to unit variance, for example.

Random Forest classification. For automated identification of behaviors across our entire video dataset (Figure 3-5, Figure S3-5), we trained supervised random forest classifiers using manually annotated data. Behaviors of interest during defeat included being attacked, being investigated, fighting back, fleeing, and being vigilant. These each were classified by a separate binary random forest classifier (Scikit-learn). The training and testing set consisted of twenty videos each. Ground truth was determined by manual annotation (BORIS) for frames in which the behavior was occurring (see above).

For each classified behavior, the feature matrix included the 12 features described above for each video frame. The objective matrix was a binary indicator if the behavior was manually annotated in that frame. The training set was composed of all the frames in which the behavior was present and a randomly selected equal number of frames in which the behavior was absent. The classifier was trained with a maximum depth of 2 and 100 estimators.

The probability threshold for detecting behaviors was set to the most permissive possible without exceeding a false positive rate of 3% on the training set. Evaluation was conducted by plotting the receiver operator curve on the held-out testing set (Figure S3C, D).

Unsupervised behavior classification. To characterize behaviors as stereotyped features

repeated throughout time, we followed previous work[96] in using a low-dimensional embedding of the original features and defining behaviors as high density clusters in that low-dimensional embedding to create Figure 3C. To achieve dense clusters, we embedded our behavior features using *t*-SNE, which preserves small pairwise distances and thereby retains clustering of nearby points.

Generating this manifold involved a technique known as importance sampling, which enabled us to create a final embedding that included behaviors that might be rare or nuanced, and therefore under-represented in a uniform sampling over time. Importance sampling includes two rounds of *t*-SNE embedding. First, around 12,000 frames of behavior were uniformly sampled in time across all videos (N =350) analyzed. Those features were embedded into a two-component *t*-SNE manifold (sklearn.manifold.TSNE with perplexity = 100). The embedded space was binned into a 50 × 50 histogram, smoothed with a 2D Gaussian kernel (with a standard deviation of 2.5), and parcellated into 17 clusters with watershed (skimage.morphology.watershed) over the smoothed histogram. When then used a multilayer perceptron (sklearn.neural_network.MLPRegressor, hidden layer size of 400 × 200 × 50 units) to represent data from every video frame in 2D *t*-SNE space, and thus to fall into 1 of the 17 clusters defined in this space.

Because we are interested in attack behaviors, we repeated these steps but with a subset of frames that were biased to have more attack frames. To sample from aggressive behavior, we characterized the overlap between random forest-classified attack frames and the clusters in *t*-SNE space. From the cluster that most overlapped with attack, we sampled five random frames from every defeat session. From the 16 remaining non-attack clusters, we sampled 2 random frames from every defeat session. Thus, from 35 males undergoing defeat for 10 days, we sampled (2 × 16) frames from non-attack clusters and 5 frames from the attack cluster on each day for each mouse for a total of 35 × 10 × (16 × 2 + 5) = 12,950 frames. From these sampled frames, we again embedded the 12-dimensional behavior features into two-component *t*-SNE space. The full set of video frames was then mapped into this final *t*-SNE manifold using another multilayer perceptron. Then a 2D histogram of that perceptron-mapped 2D data was smoothed with a Gaussian kernel (with a standard deviation of 1.5) and divided into 17 clusters again with watershed. Gaussian kernels in both *t*-SNE steps were chosen by rounding to the nearest 0.5 and to yield 10–20 clusters from watershed clustering.

To plot behavior data from our optogenetics experiments in the same *t*-SNE space (Figure 5E), the perceptron (sklearn.neural_network.MLPRegressor) used to learn the 12 features from the fiber photometry experiments to create the *t*-SNE mapping (Figure 3C) was applied to the 12 features from the optogenetics experiments in the same way.

Neural analysis

Processing of fiber photometry data. For Figure 2, raw fluorescence data in each session was converted into dF/F using a moving average (window of 30s) to calculate F_0. The data was then z-scored by diving by the standard deviation of the dF/F signal across the entire session. For Figures 3-4, defeat recordings for each mouse were converted into dF/F using the average of each session rather than a moving window to calculate F_0. Sessions were then appended and z-scoring was performed by dividing by the standard deviation of all 10 days of defeat.

Pre-processing of cellular resolution calcium imaging data. Initial pre-processing was done in IDPS 1.8.0 (Inscopix Data Processing Software). Videos were spatially downsampled by a

factor of 4 and motion-corrected with a translational correction algorithm based on cross-correlations computed on consecutive frames. Videos were subsequently exported as .tiff files and further motion-corrected using NoRMCorre[97]. After motion correction, the CNMFe algorithm[98,99] was used to identify neurons and obtain their fluorescence traces. The fluorescence traces were then z-scored using the same method as for the fiber photometry data described above.

Plotting neural data in behavioral t-SNE space. We wanted to see the corresponding neural activity within the behavioral clusters identified from the t-SNE map in Figure 3D, 4A-C). Because peak neural activity to proximity-related behaviors occurred 0.5 s after the start of attack (Figure 3K-N), we shifted the fluorescent data of each video forward 0.5 s. We then identified the neural activity corresponding with each video frame and also where that video frame is located in the 50 x 50 t-SNE embedding. Then we smoothed the neural data plotted in t-SNE space with a 2D Gaussian kernel (with a standard deviation of 1.5).

Brainwide Fos analysis (Figure 6)

Behavior. Mice were placed for 10 min into the cage of a novel Swiss Webster aggressor that was restrained under a wire cup and were then sacrificed one hour later for fos analysis. Mice were deeply anesthetized (2 mg/kg Euthasol ip.) and then transcardially perfused with ice-cold PBS + heparin (20 U/mL; Sigma H3149) followed by ice-cold 4% PFA in PBS. Brains were then extracted and post-fixed overnight in 4% PFA at 4°C.

For analysis of susceptible vs resilient groups, mice were defined as susceptible if their social interaction time in the SI test was less than one standard deviation below that of unstressed controls (from our fiber photometry dataset, Figure 1B), otherwise they were considered resilient.

Tissue clearing and immunolabeling. Brains were cleared and immunolabeled using an iDISCO+ protocol as previously described[52,53]. All incubations were performed at room temperature unless otherwise noted.

Clearing: Brains were serially dehydrated in increasing concentrations of methanol (Carolina Biological Supply 874195; 20%, 40%, 60%, 80%, 100% in doubly distilled water (ddH2O); 45 min–1 h each), bleached in 5% hydrogen peroxide (Sigma H1009) in methanol overnight, and then serially rehydrated in decreasing concentrations of methanol (100%, 80%, 60%, 40%, 20% in ddH2O; 45 min–1 h each).

Immunolabeling: Brains were washed in 0.2% Triton X-100 (Sigma T8787) in PBS, followed by 20% DMSO (Fisher Scientific D128) + 0.3 M glycine (Sigma 410225) + 0.2% Triton X-100 in PBS at 37°C for 2 d. Brains were then washed in 10% DMSO + 6% normal donkey serum (NDS; EMD Millipore S30) + 0.2% Triton X-100 in PBS at 37°C for 2–3 d to block non-specific antibody binding. Brains were then twice washed for 1 h at 37°C in 0.2% Tween-20 (Sigma P9416) + 10 mg/mL heparin in PBS (PTwH solution) followed by incubation with primary antibody solution (rabbit anti-Fos, 1:1000; Synaptic Systems 226008; chicken anti-GFP, 1:500; Aves GFP-1020) in 5% DMSO + 3% NDS + PTwH at 37°C for 7 d. Brains were then washed in PTwH 6× for increasing durations (10 min, 15 min, 30 min, 1 h, 2 h, overnight) followed by incubation with secondary antibody solution (Alexa Fluor 647 donkey anti-rabbit, 1:200; Abcam ab150075; Alexa Fluor 594 donkey anti-chicken, 1:500; Jackson Immuno 703-585-155) in 3%

NDS + PTwH at 37°C for 7 d. Brains were then washed in PTwH 6× for increasing durations again (10 min, 15 min, 30 min, 1 H, 2 H, overnight).

Final storage and imaging: Brains were serially dehydrated in increasing concentrations of methanol (20%, 40%, 60%, 80%, 100% in ddH2O; 45 min–1 h each), then incubated in a 2:1 solution of dichloromethane (DCM; Sigma 270997) and methanol for 3 h followed by 2× 15-min washes 100% DCM. Before imaging, brains were stored in the refractive index-matching solution dibenzyl ether (DBE; Sigma 108014).

Fos light sheet imaging. Cleared and immunolabeled brains were glued (Loctite 234796) ventral side-down to a 3D-printed holder and imaged in DBE using a dynamic axial sweeping light sheet fluorescence microscope (Life Canvas SmartSPIM). Images were acquired using a 3.6×/0.2 NA objective with a 3,650 μm×3,650 μm field-of-view onto a 2,048 px×2,048 px sCMOS camera (pixel size: 1.78 μm×1.78 μm) with a spacing of 2 μm between horizontal planes (nominal z-dimension point spread function: 3.2–4.0 μm). Imaging the entire brain required 4×6 tiling across the horizontal plane and 3,300–3,900 total horizontal planes. Autofluorescence channel images were acquired using 488 nm excitation light at 20% power and 2ms exposure time, Fos channel images were acquired using 639 nm excitation light at 90% power and 2ms exposure time, and YFP channel images were acquired using 561 nm excitation light at 20% power and 2-ms exposure time to confirm ChR2-YFP expression.

After acquisition, tiled images for the Fos channel were first stitched into a single imaging volume using the TeraStitcher C++ package (https://github.com/abria/TeraStitcher). These stitching parameters were then directly applied to the tiled autofluorescence channel images, yielding two aligned 3D imaging volumes with the same final dimensions. After tile stitching, striping artifacts were removed from each channel using the Pystripe Python package (https://github.com/chunglabmit/pystripe).

We registered the final Fos imaging volume to the Allen CCF using the autofluorescence imaging volume as an intermediary. We first downsampled both imaging volumes by a factor of 5 for computational efficiency. Autofluorescence→atlas alignment was done by applying an affine transformation to obtain general alignment using only translation, rotation, shearing, and scaling, followed by applying a b-spline transformation to account for local nonlinear variability among individual brains. Fos→autofluorescence alignment was done by applying only affine transformations to account for brain movement during imaging and wavelength-dependent aberrations. Alignment transformations were computed using the Elastix C++ package (https://github.com/SuperElastix/elastix). These transformations allowed us to transform Fos^+ cell coordinates first from their native space to the autofluorescence space and then to Allen CCF space.

Deep learning-assisted cell detection pipeline. We first use standard machine vision approaches to identify candidate Fos^+ cells based on peak intensity and then use a convolutional neural network to remove artifacts. Our pipeline builds upon the ClearMap Python package[52,53] (https://github.com/ChristophKirst/ClearMap2) for identifying candidate cells and the Cellfinder Python package[100] (https://github.com/brainglobe/cellfinder) for artifact removal.

Cell detection: ClearMap operates through a series of simple image processing steps. First, the Fos imaging volume is background-subtracted using a morphological opening (disk size: 21 px).

Second, potential cell centers are found as local maxima in the background-subtracted imaging volume (structural element shape: 11 px). Third, cell size is determined for each potential cell center using a watershed algorithm (see below for details on watershed detection threshold). Fourth, a final list of candidate cells is generated by removing all potential cells that are smaller than a preset size (size threshold: 350 px). We confirmed that our findings were consistent across a wide range of potential size thresholds.

We implemented three changes to the standard ClearMap algorithm. First, we de-noised the Fos imaging volume using a median filter (function: scipy.ndimage.median_filter; size: 3 px) before the background subtraction step. Second, we dynamically adjusted the watershed detection threshold for each sample based on its fluorescence intensity. This step was important for achieving consistent cell detection performance despite changes in background and signal intensity across batches and samples due to technical variation in clearing, immunolabeling, and imaging. Briefly, we selected a 1,000 px×1,000 px×200 px subvolume at the center of each sample's Fos imaging volume. We then median filtered and background subtracted this subvolume as described above. We then used sigma clipping (function: astropy.stats.sigma_clipped_stats; sigma=3.0, maxiters=10, cenfunc='median', stdfunc='mad_std') to estimate the mean background (non-cell) signal level for this subvolume, μ_{bg}, and set each sample's watershed detection threshold to $10*\mu_{bg}$. Third, we removed from further analysis all cell candidates that were located outside the brain, in the anterior olfactory areas or cerebellum (which were often damaged during dissection), or in the ventricles, fiber tracts, and grooves following registration to the Allen CCF.

Cell classification: One limitation of the watershed algorithm implemented by ClearMap is that it identifies any high-contrast feature as a candidate cell, including exterior and ventricle brain edges, tissue tears, bubbles, and other aberrations. To overcome this limitation, we re-trained the 50-layer ResNet implemented in Keras (https://keras.io) for TensorFlow (https://www.tensorflow.org) from the Cellfinder Python package to classify candidate Fos^+ cells in our high-resolution light sheet imaging dataset as true Fos^+ cells or artifacts. This network uses both the autofluorescence and Fos channels during classification because the autofluorescence channel has significant information about high-contrast anatomical features and imaging aberrations. We first manually annotated 2,000 true Fos^+ cells and 1,000 artifacts from each of four brains across two technical batches using the Cellfinder Napari plugin, for a total training dataset of 12,000 examples. We then re-trained the Cellfinder network (which had already been trained on 2p images of GFP^+ cells) using TensorFlow over 100 epochs with a learning rate of 0.0001 and 1,200 examples (10% of the training dataset) held out for validation. Re-training took 4 d 16 min 41 sec on a high performance computing cluster using 1 GPU and 12 CPU threads. We achieved a final validation accuracy of 98.33%. Our trained convolutional neural network removed 15.99% ± 0.58% (mean ± s.e.m.; range: 2.96% – 32.71%; n = 99 brain[54]) of cell candidates from ClearMap as artifacts.

Atlas registration: We used the ClearMap interface with Elastix to transform the coordinates of each true Fos^+ cell to Allen CCF space using the transformations described above. We then used these coordinates to assign each Fos^+ cell to an Allen CCF brain region. For each sample, we generated a final data structure containing the Allen CCF coordinates (*x*,*y*,*z*), size, and brain region for each true Fos^+ cell.

Fos density maps. We generated 3D maps of Fos^+ cell density by applying a gaussian kernel-density estimate (KDE) (function: *scipy.stats.gaussian_kde*) in Python to all Fos^+ cells

across all animals within a given experimental condition (for example, susceptible mice). These maps are visualized in Figure 6D (interactive visualization: https://www.brainsharer.org/ng/?id=876) .

We first generated a table containing the Allen CCF coordinates (*x*,*y*,*z*) for every Fos^+ cell in every animal within an experimental condition. At this stage, we listed each cell twice (once with its original coordinates and once with its ML (*z*) coordinate flipped to the opposite hemisphere) in order to pool data from both hemispheres. We used a modified symmetrical version of the Allen CCF to facilitate this. We then assigned each cell a weight equal to the inverse of the total number of Fos^+ cells in that animal to ensure that each animal within an experimental condition would be weighted equally. We then fit a 3D gaussian KDE for each experimental condition using the scipy.stats.gaussian_kde function, and manually set the kernel bandwidth for every experimental condition to be equal at 0.04. We then evaluated this KDE at every voxel in the Allen CCF (excluding voxels outside the brain or in anterior olfactory areas, cerebellum, ventricles, fiber tracts, grooves) to obtain a 3D map of Fos^+ density for each condition. Lastly, we normalized the KDE for each experimental condition by dividing by its sum as well as the voxel size of the atlas, $(0.025\ mm)^3$, to generate a final 3D map with units of "% Fos^+ cells per mm^3". To examine the difference in Fos^+ cell density across conditions, we simply subtracted the 3D KDE volumes for the two conditions, e.g. Resilient – Susceptible, and then plotted coronal sections through this subtracted volume with Allen CCF boundaries overlaid. The colorbar limits for all KDE figures are ±0.5% Fos^+ cells per mm^3.

Fos GLMs. We adopted a GLMM to analyze the Fos data in the LHb stimulation cohort (Figure 6E-J). This allowed us to model the contribution of SI time (time near aggressor) or ChR2/YFP to neural activation in each brain region, while also accounting for the overdispersed, discrete nature of the data by employing a negative binomial link function. We first fit a GLM for each brain region using the glmmTMB R package (https://github.com/glmmTMB/glmmTMB) with a *nbinom2* link function and the formula, **Counts ~ SI_time + ln(TotalCounts)**, where **Counts** is the number of Fos^+ cells in a brain region, **SI_time** is an animal's Social Interaction Test score, and **ln(TotalCounts)** is an offset term for the total number of Fos^+ cells in each sample. We used the coefficient estimate and standard error (*Z*-value = estimate/standard error) as a proxy for modulation by susceptibility and resilience. We calculated a *p*-value for each brain region using this statistic, and corrected for a 10% false discovery rate across all brain regions using the Benjamini-Krieger-Yekutieli two-step procedure. Brain regions that passed this false discovery rate threshold are highlighted in Figure 6E.

For the LHb stimulation cohort, we then fit similar regressions using **ChR2** (a categorical variable, 1 for YFP and 0 for ChR2) as a regressor instead of SI_time, and then calculated *Z*-values (coefficient estimate/standard error) for each of these variables. We also performed a control CSDS experiment with mice that did not have any LHb stimulation and repeated the analysis described above (Figure 6H).

In Figure 6F-H, we used the Violinplot MATLAB package (https://github.com/bastibe/Violinplot-Matlab) to plot the distribution of Z-values described above for all brain regions in cortex (Cerebral Cortex, by Allen designation) and subcortical nuclei (Cerebral Nuclei, Thalamus, Hypothalamus, Midbrain, Pons, Medulla, by Allen designation). We used Kolmogorov-Smirnov tests to assess whether these distributions were significantly different from each other in cortex vs subcortex.

In Figure 6I, we took the pairwise correlation across brain regions for the SI time regressor *Z*-scores for the control cohort and the SI time regressor *Z*-scores for the LHb stimulation cohort. In Figure 6J, we took the pairwise correlation across brain regions for the SI time regressor *Z*-scores for the control cohort and the **ChR2** regressor *Z*-scores for the LHb stimulation cohort.

Data and code availability

All data and code used to generate the figures in this paper will be made publicly available upon publication.

Acknowledgments

We thank Esteban Engel, Oliver Huang, Angela Chan, and the PNI Viral Core Facility for AAV production; Jeffrey Stirman and Life Canvas Technologies for light sheet imaging support; the Kleinfeld and Wang labs for collaboration on the Brainsharer web portal; Adrian Sirko and the Princeton Laboratory Animal Resources staff for help with animal husbandry; and C. Peña, M. Murthy, Rob Fetcho, Adelaide Minerva, and other members of the Witten lab for feedback on this work. This work was supported by NIH 1DP1MH136573 (IBW), the Simons Collaboration on the Global Brain (IBW, AF), HHWF (CAZ), Princeton Innovation Fund (IBW, AF), and the New York Stem Cell Foundation (IBW, AF).

Author contributions

A.Z. and I.B.W. conceived the project, designed the experiments, and interpreted the data, with input from L.W. and A.L.F. A.Z. collected and analyzed the majority of the data. S.N.J. collected the data for Figure 6. L.W. provided code and advised on analysis for Figure 3-5. C.A.Z. analyzed data for Figure 6. I.B.W. advised on the data analysis. A.Z., C.A.Z. and I.B.W. wrote the paper.

Competing interests

The authors declare no competing interests.

Supplemental Figures and Data Tables

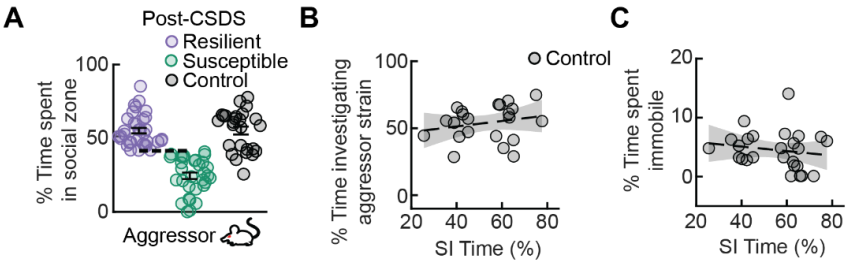

Supplementary Figure 1. Additional data related to Figure 1. A. Post-CSDS time spent near the social target in SI test when the social target was of the aggressor strain. **B**. Relationship between time spent investigating a juvenile from the aggressor strain in the homecage assay and aggressor strain SI time for control mice that did not undergo defeat: $R = 0.2177$, $p = 0.3305$. **C**. Relationship between time spent immobile during chamber exploration and SI time for control mice that did not undergo defeat: $R = -0.1650$, $p = 0.4205$. *p*-values in **B**, **C** are from Pearson's correlation. Shaded areas in **B**, **C** represent 95% confidence interval for linear fit. See Table 1 for detailed statistics summary.

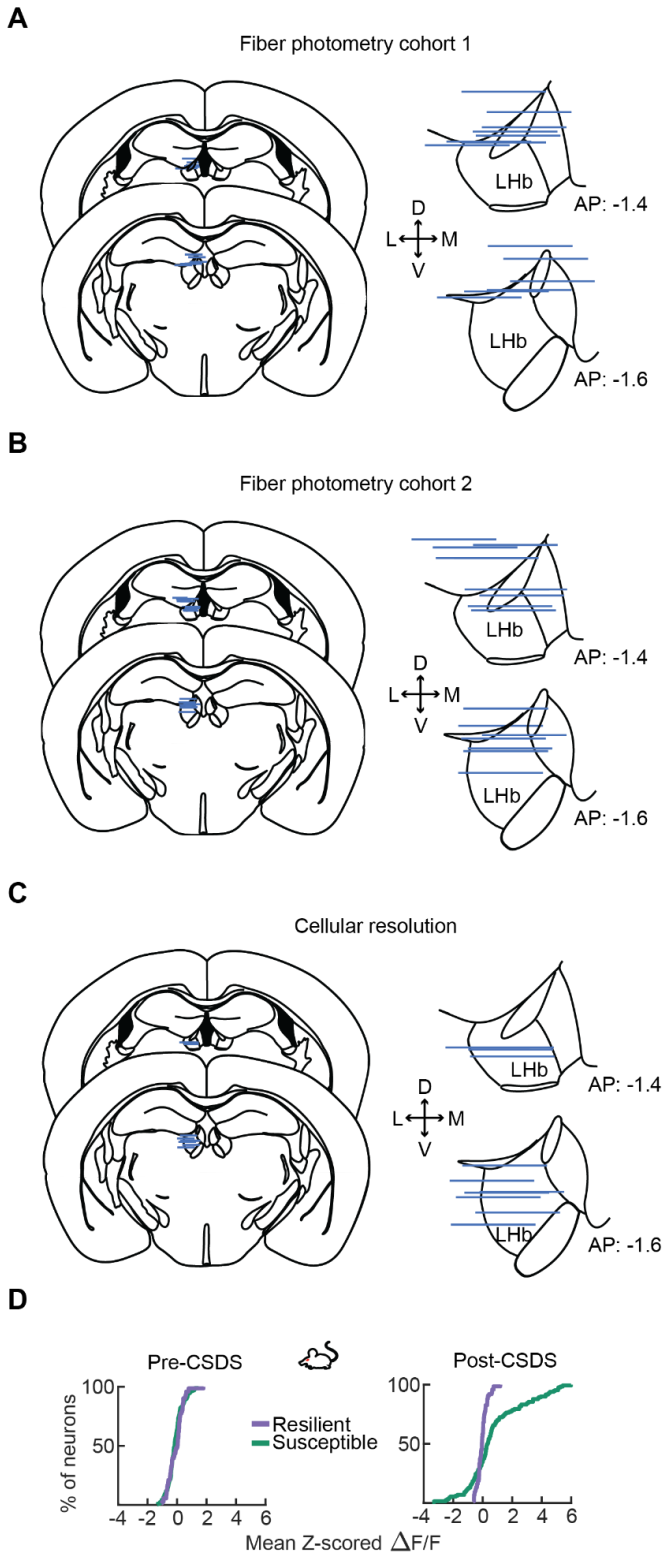

Supplementary Figure 2. Additional data related to Figure 2. A. Left: Histology summary of fiber tips for first photometry cohort (all plotted on left hemisphere for visualization). Right: Zoom in on LHb for fiber locations. **B**. Left: Histology summary of fiber tips for second photometry cohort (all plotted on left hemisphere for visualization). Right: Zoom in on LHb for fiber locations. **C**. Left: Histology summary of

fiber tips for all cellular resolution calcium imaging mice (all plotted on left hemisphere for visualization). Right: Zoom in on LHb for fiber locations. **D**. CDF of responses to aggressor strain proximity for susceptible and resilient neurons before CSDS (left) and after CSDS (right).

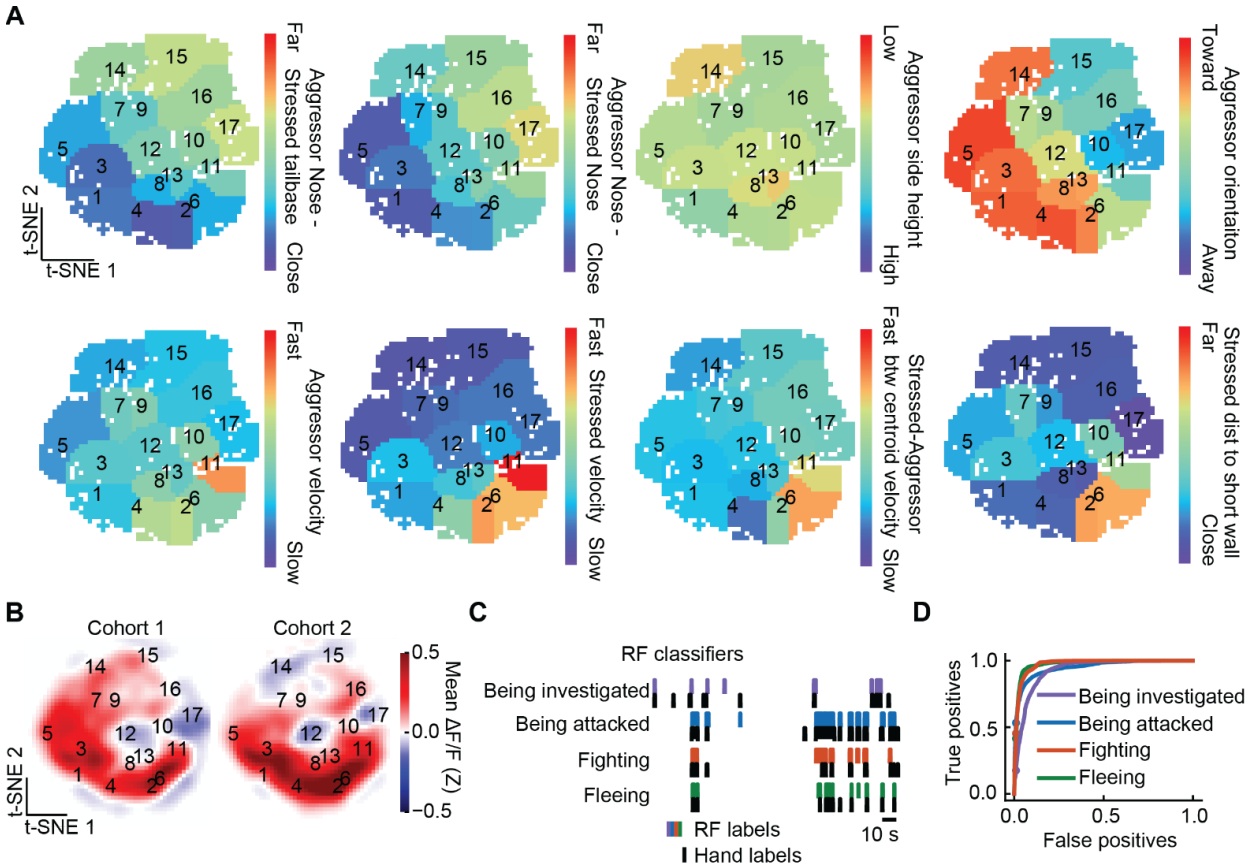

Supplemental Figure 3. Additional data related to Figure 3. A. Average raw feature value within each *t*-SNE cluster. **B**. Mean LHb GCaMP responses across *t*-SNE behavior space in defeated mice plotted separately for each cohort (cohort 1: AAV5-CaMKII-GCaMP6f; cohort 2: AAV5-syn-jGCaMP7f). **C**. Comparison of hand-labeled behavior to performance of binary random forest (RF) classification of behaviors. **D**. Accuracy of behavior classification.

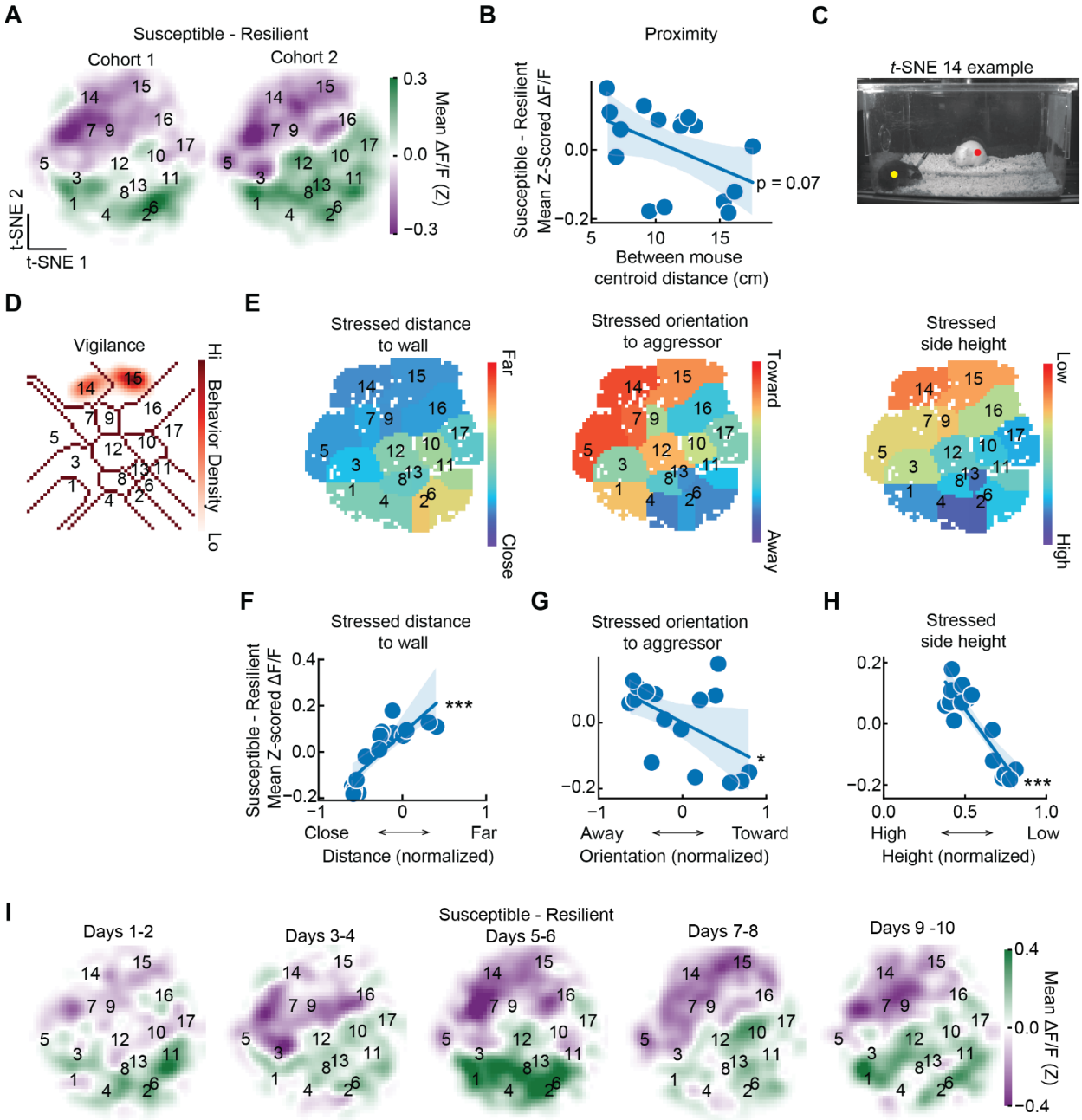

Supplemental Figure 4. Additional data related to Figure 4 A. Difference between susceptible and resilient maps of mean LHb GCaMP responses across *t*-SNE behavior space for each cohort. **B**. Difference between susceptible and resilient mean LHb GCaMP of each cluster plotted against mean centroid distance between mice of each cluster (N = 17 clusters). R = 0.466, p = 0.069. **C**. Example frame from cluster 14. **D**. Density of vigilance behavior annotated with supervised classifiers within *t*-SNE space. **E**. Average raw feature value within *t*-SNE clusters that have a similar pattern to the susceptible-resilient GCaMP activity map. **F**. Difference between susceptible and resilient mean LHb GCaMP of each cluster plotted against stressed mouse distance to closest wall (N = 17 clusters). R = 0.8349, p = 5.7E-5. **G**. Difference between susceptible and resilient mean LHb GCaMP of each cluster plotted against stressed mouse orientation to aggressor (N = 17 clusters). R = 0.532, p = 0.0339. **H**. Difference between susceptible and resilient mean LHb GCaMP of each cluster plotted against stressed mouse side height (N = 17 clusters). R = -0.8952, p = 2.8E-6. **I**. Evolution of susceptible-resilient GCaMP activity mapped onto *t*-SNE behavior space across defeat. *p*-values in **B**, **F**-**H** are from Pearson's correlation. Shaded areas in

B, **F**-**H** represent 95% confidence interval for linear fit. *$p \leq 0.05$, **$p \leq 0.01$, ***$p \leq 0.001$. See Table 1 for detailed statistics summary.

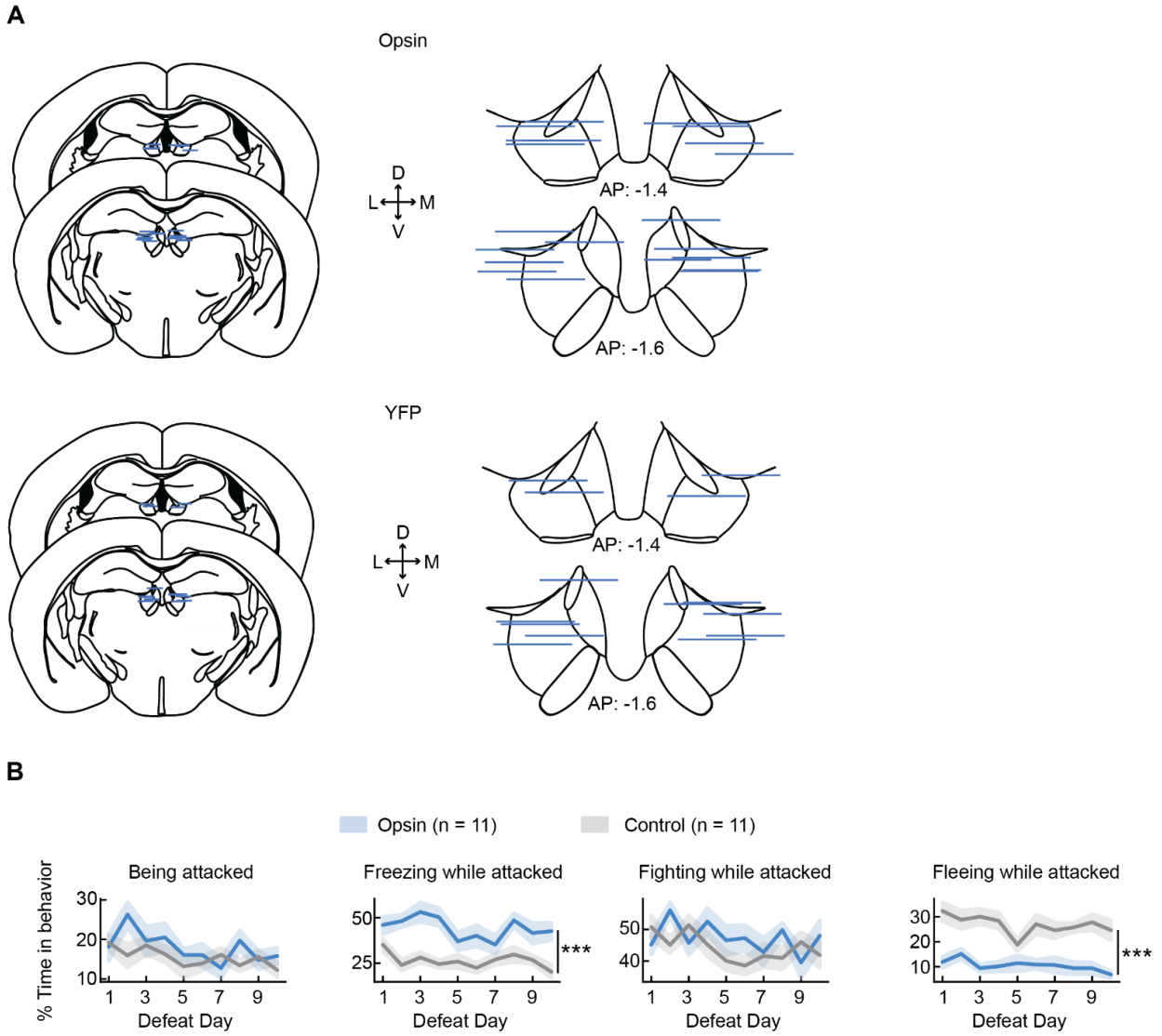

Supplemental Figure 5. Additional data related to Figure 5. A. Histology summary of implant targeting. **B**. Time spent in classified behaviors across days (mean ± s.e.m. plotted). Time attacked: effect of opsin group $Z = -1.831$, $p = 0.0687$, effect of day $Z = -1.897$, $p = 0.058$, interaction, $Z = 0.405$, $p = 0.685$; Freezing while attacked: effect of opsin group $Z = -4.956$, $p < 0.001$, effect of day $Z = -2.109$, $p = 0.035$, interaction, $Z = -0.177$, $p = 0.859$; Fighting while attacked: effect of opsin group $Z = -0.399$, $p = 0.690$, effect of day $Z = -0.273$, $p = 0.785$, interaction, $Z = -0.772$, $p = 0.440$; Fleeing while attacked: effect of opsin group $Z = 8.721$, $p = <0.001$, effect of day $Z = -2.740$, $p = 0.006$, interaction, $Z = 0.111$, $p = 0.912$. *p*-values in **B** are from two-sided GEE. *$p \leq 0.05$, **$p \leq 0.01$, ***$p \leq 0.001$. See Tables 10-13 for more information on GEE statistics.

Supplementary Data Table 1: **Statistics summary**
Note: all t-tests and correlations are 2-sided unless noted otherwise. In “Significance” column: *p<0.05, **p<0.01, ***p<0.001, NS not significant.

Figure	Description	Sample size	Statistical test	Test Statistic	*p* Value	Significance
Figure 1B	Self strain SI time in susceptible mice pre-CSDS vs post-CSDS	26 mice, 26 mice	Paired t-test (with Bonferroni correction)	t = -6.1047	<0.0001	***
Figure 1C	Investigation time difference across stress groups to aggressor strain in homecage assay	68 mice, 3 groups	1-way ANOVA	$F_{(65,2)} = 5$	0.0096	**
Figure 1C	Investigation time difference across susceptible and resilient to aggressor strain in homecage assay	26 mice, 20 mice	t-test	t = -2.1898	0.0339	*
Figure 1C	Investigation time difference across susceptible and control to aggressor strain in homecage assay	26 mice, 22 mice	t-test	t = -3.2324	0.0023	**
Figure 1C	Investigation time difference across resilient and control to aggressor strain in homecage assay	22 mice, 22 mice	t-test	t = -0.3753	0.7095	NS
Figure 1C	Investigation time difference across stress groups to self strain in homecage assay	67 mice, 3 groups	1-way ANOVA	$F_{(64,2)} = 3.16$	0.0491	*
Figure 1C	Investigation time difference across susceptible and resilient to self strain in homecage assay	26 mice, 19 mice	t-test	t = 2.0548	0.0460	*
Figure 1C	Investigation time difference across susceptible and control to self strain in homecage assay	26 mice, 22 mice	t-test	t = 2.1285	0.0387	*
Figure 1C	Investigation time difference across resilient and control to self strain in homecage assay	19 mice, 22 mice	t-test	t = -0.122	0.9037	NS

Figure 1D	Time spent investigating aggressor strain juvenile in homecage vs SI time	46 mice	Pearson's correlation	R = 0.3965	0.0064	**
Figure 1E	Open arm time difference across susceptible vs resilient	11 mice, 20 mice	t-test	t = -2.1745	0.038	*
Figure 1F	Open arm time vs SI time	31 mice	Pearson's correlation	R = 0.5118	0.0032	**
Figure 1G	Latency to feed difference across susceptible vs resilient	10 mice, 20 mice	t-test	t = 2.4426	0.0212	*
Figure 1H	Latency to feed vs SI time	30 mice	Pearson's correlation	R = -0.6323	0.0002	***
Figure 1I	Immobility difference across susceptible vs resilient	31 mice, 35 mice	t-test	t = -2.1302	0.037	*
Figure 1J	Immobility vs SI time	66 mice	Pearson's correlation	R = -0.3757	0.0019	**
Figure 2F	LHb(GCaMP) at social zone entry	28 mice	Paired t-test (with Bonferroni correction)	t = -4.1216	0.0078	**
Figure 2O	LHb(GCaMP) at social zone entry	131 neurons from 5 mice, 75 neurons from 4 mice	t-test (with Bonferroni correction)	t = -5.7393	<0.0001	***
Figure 3F	LHb(GCaMP) mean of each cluster vs mean distance between mice of each cluster	17 clusters	Pearson's correlation	R = -0.8210	5.4E-5	***
Figure 4L	LHb(GCaMP) at attack onset on day 1 vs SI time	21 mice	Pearson's correlation	R = -0.5571	0.0087	**
Figure 4M	LHb(GCaMP) at fighting onset on day 1 vs SI time	21 mice	Pearson's correlation	R = -0.4374	0.0474	*
Figure 4N	LHb(GCaMP) at fleeing onset on day 1 vs SI time	21 mice	Pearson's correlation	R = -0.5580	0.0086	**
Figure 4O	LHb(GCaMP) at vigilance onset on day 1 vs SI time	21 mice	Pearson's correlation	R = 0.4931	0.0231	*

Figure 5G	SI time difference across opsin vs YFP	11 mice, 11 mice	t-test	t = -2.1263	0.0461	*
Figure 5H	Inner zone time difference across opsin vs YFP	11 mice, 11 mice	t-test	t = -2.8231	0.0105	*
Figure 5I	Open arm time difference across opsin vs YFP	11 mice, 11 mice	t-test	t = -2.2934	0.0328	*
Figure 6F	Difference in SI time coefficient distributions, cortex vs subcortical nuclei	61 regions, 139 regions	Kolmogorov-Smirnov test	ks = 0.448	4.0E-8	***
Figure 6G	Difference in ChR2/YFP coefficient distributions, cortex vs subcortical nuclei	61 regions, 139 regions	Kolmogorov-Smirnov test	ks = 0.472	5.8E-9	***
Figure 6H	Difference in SI time coefficient distributions, cortex vs subcortical nuclei (for control cohort)	61 regions, 139 regions	Kolmogorov-Smirnov test	ks = 0.288	0.0018	**
Figure 6I	Estimated SI time contributions to Fos^+ cell counts (control cohort) vs estimated SI time contributions to Fos^+ cell counts (LHb stimulation cohort)	200 regions	Pearson's correlation	r = 0.185	0.0088	**
Figure 6J	Estimated SI time contributions to Fos^+ cell counts (control cohort) vs. estimated ChR2 contributions to Fos^+ cell counts (LHb stimulation cohort)	200 regions	Pearson's correlation	r = 0.143	0.043	*
Supp. Figure 1B	Time spent investigating aggressor strain juvenile in homecage vs SI time for control mice	26 mice	Pearson's correlation	R = 0.2177	0.3305	NS
Supp. Figure 1C	Immobility vs SI time for control mice	26 mice	Pearson's correlation	R = -0.1650	0.4205	NS
Supp. Figure 4B	Difference in LHb(GCaMP) mean of each cluster vs mean distance between mice of each cluster	17 clusters	Pearson's correlation	R = 0.466	0.069	NS

Supp. Figure 4F	Difference in LHb(GCaMP) mean of each cluster vs mean distance from closest wall of each cluster	17 clusters	Pearson's correlation	R = 0.8349	5.7E-5	***
Supp. Figure 4G	Difference in LHb(GCaMP) mean of each cluster vs mean stressed mouse orientation to aggressor mouse of each cluster	17 clusters	Pearson's correlation	R = -0.532	0.0339	*
Supp. Figure 4H	Difference in LHb(GCaMP) mean of each cluster vs mean stressed mouse side height of each cluster	17 clusters	Pearson's correlation	R = -0.8952	2.8E-6	***

Supplementary Data Table 2: 2-sided GEE regression of LHb GCaMP (**Figure 4H**): Z-scored LHb GCaMP ΔF/F at attack onset = defeat day + SI time + defeat day*SI time + intercept, grouped by mouse. Number of mice (groups) = 21, minimum samples per group 10, maximum samples per group 11, dependence structure = independence, family = Gaussian. NOTE: defeat day and SI time are coded as mean centered.

Model: ***attack onset*** *Z-scored LHb (GCaMP) ΔF/F = defeat day + SI time + defeat day*SI time + intercept*	**β±standard error**	**z-stat**	**p-value**	**95% CI [lower, upper]**	
Intercept	0.6615±0.064	10.311	<0.001	0.536	0.787
Defeat day	0.0065±0.014	0.483	0.629	-0.020	0.033
SI time	-0.0066±0.003	-2.529	0.011	-0.012	-0.001
Defeat day * SI time	0.0011±0.001	2.066	0.039	5.85e-05	0.002

Supplementary Data Table 3: 2-sided GEE regression of LHb GCaMP (**Figure 4H**): Z-scored LHb GCaMP ΔF/F at attack onset = defeat day + susceptibility category + defeat day*susceptibility category + intercept, grouped by mouse. Number of mice (groups) = 21, minimum samples per group 10, maximum samples per group 11, dependence structure = independence, family = Gaussian. NOTE: defeat day is coded as mean centered.

Model: ***attack onset*** *Z-scored LHb (GCaMP) ΔF/F = defeat day + susceptibility category + defeat day*susceptibility category + intercept*	**β±standard error**	**z-stat**	**p-value**	**95% CI [lower, upper]**

Intercept	0.8046±0.099	8.134	<0.001	0.611	0.999
Defeat day	-0.0172±0.025	-0.688	0.491	-0.066	0.032
Susceptibility category	-0.2938±0.128	-2.295	0.022	-0.545	-0.043
Defeat day * Susceptibility category	0.0509±0.026	1.933	0.053	-0.001	0.102

Supplementary Data Table 4: 2-sided GEE regression of LHb GCaMP (**Figure 4l**): Z-scored LHb GCaMP ΔF/F at fighting onset = defeat day + SI time + defeat day*SI time + intercept, grouped by mouse. Number of mice (groups) = 21, minimum samples per group 10, maximum samples per group 11, dependence structure = independence, family = Gaussian. NOTE: defeat day is coded as mean centered.

Model: ***fighting onset*** *Z-scored LHb (GCaMP) ΔF/F = defeat day + SI time + defeat day*SI time + intercept*	**β±standard error**	**z-stat**	**p-value**	**95% CI [lower, upper]**	
Intercept	0.7821±0.091	8.567	<0.001	0.603	0.961
Defeat day	-0.0064±0.014	-0.446	0.655	-0.035	0.022
SI time	-0.0074±0.004	-2.063	0.039	-0.014	-0.000
Defeat day * SI time	0.0005±0.001	0.840	0.401	-0.001	0.002

Supplementary Data Table 5: 2-sided GEE regression of LHb GCaMP(**Figure 4l**): Z-scored LHb GCaMP ΔF/F at fighting onset = defeat day + susceptibility category + defeat day*susceptibility category + intercept, grouped by mouse. Number of mice (groups) = 21, minimum samples per group 10, maximum samples per group 11, dependence structure = independence, family = Gaussian. NOTE: defeat day is coded as mean centered.

Model: ***fighting onset*** *Z-scored LHb (GCaMP) ΔF/F = defeat day + susceptibility category + defeat day*susceptibility category + intercept*	**β±standard error**	**z-stat**	**p-value**	**95% CI [lower, upper]**	
Intercept	0.9577±0.134	7.130	<0.001	0.694	1.221
Defeat day	-0.0141±0.026	-0.544	0.587	-0.065	0.037
Susceptibility category	-0.3602±0.179	-2.014	0.044	-0.711	-0.010
Defeat day * Susceptibility category	0.0173±0.028	0.612	0.540	-0.038	0.073

Supplementary Data Table 6: 2-sided GEE regression of LHb GCaMP (**Figure 4J**): Z-scored LHb GCaMP ΔF/F at fleeing onset = defeat day + SI time + defeat day*SI time + intercept, grouped by mouse. Number of mice (groups) = 21, minimum samples per group 10, maximum samples per group 11, dependence structure = independence, family = Gaussian. NOTE: defeat day is coded as mean centered.

Model: ***fleeing onset*** *Z-scored LHb (GCaMP) ΔF/F = defeat day + SI time + defeat day*SI time + intercept*	**β±standard error**	**z-stat**	**p-value**	**95% CI [lower, upper]**	
Intercept	0.3703±0.040	9.187	<0.001	0.291	0.449
Defeat day	-0.0049±0.010	-0.496	0.620	-0.024	0.014
SI time	-0.0036±0.002	-1.738	0.082	-0.008	0.000
Defeat day * SI time	0.0009±0.000	2.551	0.011	0.000	0.002

Supplementary DataTable 7: 2-sided GEE regression of LHb GCaMP (**Figure 4J**): Z-scored LHb GCaMP ΔF/F at fleeing onset = defeat day + susceptibility category + defeat day*susceptibility category + intercept, grouped by mouse. Number of mice (groups) = 21, minimum samples per group 10, maximum samples per group 11, dependence structure = independence, family = Gaussian. NOTE: defeat day is coded as mean centered.

Model: ***fleeing onset*** *Z-scored LHb (GCaMP) ΔF/F = defeat day + susceptibility category + defeat day*susceptibility category + intercept*	**β±standard error**	**z-stat**	**p-value**	**95% CI [lower, upper]**	
Intercept	0.4255±0.056	7.614	<0.001	0.316	0.535
Defeat day	-0.0200±0.016	-1.287	0.198	-0.051	0. 010
Susceptibility category	-0.1124±0.085	-1.321	0.186	-0.279	0.054
Defeat day * Susceptibility category	0.0323±0.020	1.584	0.113	-0.008	0.072

Supplementary Data Table 8: 2-sided GEE regression of LHb GCaMP (**Figure 4K**): Z-scored LHb GCaMP ΔF/F at vigilance onset = defeat day + SI time + defeat day*SI time + intercept, grouped by mouse. Number of mice (groups) = 21, minimum samples per group 10, maximum samples per group 11, dependence structure = independence, family = Gaussian. NOTE: defeat day is coded as mean centered.

Model: ***vigilance onset*** *Z-scored LHb (GCaMP) ΔF/F = defeat day + SI time + defeat day*SI time + intercept*	**β±standard error**	**z-stat**	**p-value**	**95% CI [lower, upper]**	
Intercept	-0.1263±0.029	-4.291	<0.001	-0.184	-0.069

Defeat day	0.0036±0.005	0.720	0.471	-0.006	0.013
SI time	0.0026±0.001	2.144	0.032	0.000	0.005
Defeat day * SI time	7.135e-05±0.000	0.313	0.754	-0.000	0.001

Supplementary DataTable 9: 2-sided GEE regression of LHb GCaMP (**Figure 4K**): Z-scored LHb GCaMP ΔF/F at vigilance onset = defeat day + susceptibility category + defeat day*susceptibility category + intercept, grouped by mouse. Number of mice (groups) = 21, minimum samples per group 10, maximum samples per group 11, dependence structure = independence, family = Gaussian. NOTE: defeat day is coded as mean centered.

*Model: **vigilance onset** Z-scored LHb (GCaMP) ΔF/F = defeat day + susceptibility category + defeat day*susceptibility category + intercept*	**β±standard error**	**z-stat**	**p-value**	**95% CI [lower, upper]**	
Intercept	-0.1904±0.046	-4.141	<0.001	-0.281	-0.100
Defeat day	0.0048±0.006	0.775	0.438	-0.007	0.017
Susceptibility category	0.1316±0.057	2.318	0.020	0.020	0.243
Defeat day * Susceptibility category	-0.0030±0.010	-0.292	0.770	-0.023	0.017

Supplementary Data Table 10: 2-sided GEE regression of behavior (**Figure S5B**, first panel): % time mice are being attacked = defeat day + opsin category + defeat day*opsin category + intercept, grouped by mouse. Number of mice (groups) = 22,minimum samples per group 11, maximum samples per group 11, dependence structure = independence, family = Gaussian. NOTE: defeat day is coded as mean centered

*Model: % time mice are **being attacked** = defeat day + opsin category + defeat day*opsin category + intercept*	**β±standard error**	**z-stat**	**p-value**	**95% CI [lower, upper]**	
Intercept	12.3172±0.583	21.121	<0.001	11.174	13.460
Defeat day	-0.6116±0.322	-1.897	0.058	-1.243	0.020
Opsin category	-1.7172±0.938	-1.831	0.067	-3.556	0.121
Defeat day * Opsin category	0.1413±0.349	0.405	0.685	-0.157	0.272

Supplementary Data Table 11: 2-sided GEE regression of behavior (**Figure S5B**, second panel): % time mice are freezing during attack = defeat day + opsin category + defeat day*opsin category + intercept, grouped by mouse. Number of mice (groups) = 22,minimum samples per group 11, maximum samples per group 11, dependence structure = independence, family = Gaussian. NOTE: defeat day is coded as mean centered

*Model: % time mice are **freezing during attack**= defeat day + opsin category + defeat day*opsin category + intercept*	**β±standard error**	**z-stat**	**p-value**	**95% CI [lower, upper]**	
Intercept	43.7667±1.883	25.898	<0.001	45.076	52.457
Defeat day	-1.1064±0.524	-2.109	0.035	-2.134	-0.078
Opsin category	-12.6126±2.545	-4.956	<0.000	-17.601	-7.625
Defeat day * Opsin category	-0.1156±0.652	-0.177	0.859	-1.394	1.162

Supplementary Data Table 12: 2-sided GEE regression of behavior (**Figure S5B**, third panel): % time mice are fighting during attack = defeat day + opsin category + defeat day*opsin category + intercept, grouped by mouse. Number of mice (groups) = 22,minimum samples per group 11, maximum samples per group 11, dependence structure = independence, family = Gaussian. NOTE: defeat day is coded as mean centered

*Model: % time mice are **fighting during attack** = defeat day + opsin category + defeat day*opsin category + intercept*	**β±standard error**	**z-stat**	**p-value**	**95% CI [lower, upper]**	
Intercept	50.1998±1.932	25.983	<0.001	46.413	53.987
Defeat day	-0.1333±0.488	-0.273	0.785	-1.090	0.823
Opsin category	-1.1085±2.775	-0.399	0.690	-6.548	-4.331
Defeat day * Opsin category	-0.4933±0.639	-0.772	0.440	-1.745	0.759

Supplementary Data Table 13: 2-sided GEE regression of behavior (**Figure S5B**, fourth panel): % time mice are fleeing during attack = defeat day + opsin category + defeat day*opsin category + intercept, grouped by mouse. Number of mice (groups) = 22,minimum samples per group 11, maximum samples per group 11, dependence structure = independence, family = Gaussian. NOTE: defeat day is coded as mean centered

*Model: % time mice are **fleeing during attack** = defeat day + opsin category + defeat day*opsin category + intercept*	**β±standard error**	**z-stat**	**p-value**	**95% CI [lower, upper]**	
Intercept	11.4885±1.582	7.263	<0.001	8.388	14.589

Defeat day	-0.6205±0.226	-2.740	0.006	-1.064	-0.177
Opsin category	16.3787±1.878	8.721	<0.001	12.698	20.060
Defeat day * Opsin category	0.0676±0.610	0.111	0.912	-1.128	1.263

Supplementary Data Table 14: GLM coefficient estimates (**Figure 6E**-**F**, **J**). The total number of Fos$^+$ cells in each brain region was modeled as ***Counts ~ SI Time + ln(Total Counts)*** using a negative binomial link function (*N* = 15 mice). The critical *p*-value for significance while permitting a 10% FDR was 0.0367.

Brain region name	**SI time coefficient estimate**	**SI time coefficient std error**	**SI time coefficient Z-statistic**	**SI time coefficient P-value**
Frontal pole	-0.058	0.012	-4.947	7.52E-07
Primary motor area	0.007	0.008	0.975	3.29E-01
Secondary motor area	0.014	0.005	2.721	6.51E-03
Primary somatosensory area, nose	0.006	0.014	0.414	6.79E-01
Primary somatosensory area, barrel field	0.024	0.009	2.585	9.74E-03
Primary somatosensory area, lower limb	0.017	0.009	1.907	5.66E-02
Primary somatosensory area, mouth	-0.006	0.015	-0.392	6.95E-01
Primary somatosensory area, upper limb	0.006	0.011	0.593	5.53E-01
Primary somatosensory area, trunk	0.012	0.006	1.929	5.37E-02
Supplemental somatosensory area	0.009	0.007	1.215	2.24E-01
Gustatory areas	-0.010	0.007	-1.497	1.34E-01
Visceral area	-0.002	0.007	-0.333	7.39E-01
Dorsal auditory area	0.019	0.010	1.814	6.97E-02
Primary auditory area	-0.002	0.008	-0.293	7.69E-01
Posterior auditory area	0.000	0.016	0.012	9.91E-01
Ventral auditory area	-0.009	0.008	-1.146	2.52E-01
Anterolateral visual area	0.038	0.014	2.648	8.09E-03
Anteromedial visual area	0.044	0.011	4.045	5.23E-05
Lateral visual area	0.042	0.014	2.972	2.96E-03
Primary visual area	0.051	0.017	2.920	3.50E-03

Posterolateral visual area	0.024	0.006	4.316	1.59E-05
Posteromedial visual area	0.043	0.014	2.975	2.93E-03
Anterior cingulate area, dorsal part	0.016	0.005	3.396	6.84E-04
Anterior cingulate area, ventral part	0.026	0.006	4.261	2.04E-05
Prelimbic area	0.003	0.009	0.321	7.48E-01
Infralimbic area	0.005	0.006	0.847	3.97E-01
Orbital area, lateral part	0.024	0.008	2.951	3.17E-03
Orbital area, medial part	-0.012	0.007	-1.755	7.92E-02
Orbital area, ventrolateral part	0.022	0.008	2.844	4.46E-03
Agranular insular area, dorsal part	0.011	0.005	2.135	3.28E-02
Agranular insular area, posterior part	0.018	0.007	2.454	1.41E-02
Agranular insular area, ventral part	0.004	0.005	0.729	4.66E-01
Retrosplenial area, lateral agranular part	0.021	0.006	3.407	6.58E-04
Retrosplenial area, dorsal part	-0.008	0.005	-1.576	1.15E-01
Retrosplenial area, ventral part	-0.001	0.006	-0.092	9.27E-01
Rostrolateral visual area	0.029	0.011	2.731	6.32E-03
Temporal association areas	-0.008	0.004	-2.207	2.73E-02
Perirhinal area	0.000	0.006	0.047	9.62E-01
Ectorhinal area	-0.007	0.007	-1.056	2.91E-01
Anterior olfactory nucleus	0.020	0.007	2.877	4.01E-03
Taenia tecta, dorsal part	0.004	0.006	0.675	5.00E-01
Taenia tecta, ventral part	-0.019	0.008	-2.308	2.10E-02
Dorsal peduncular area	0.010	0.008	1.323	1.86E-01
Piriform area	0.026	0.008	3.373	7.42E-04
Nucleus of the lateral olfactory tract	0.021	0.034	0.628	5.30E-01
Cortical amygdalar area, anterior part	0.025	0.019	1.313	1.89E-01
Cortical amygdalar area, posterior part	0.023	0.016	1.408	1.59E-01
Piriform,amygdalar area	0.000	0.009	-0.020	9.84E-01
Postpiriform transition area	0.011	0.012	0.904	3.66E-01
Field c a1	0.002	0.006	0.355	7.23E-01
Field c a2	-0.009	0.010	-0.934	3.50E-01

Field c a3	-0.001	0.007	-0.092	9.27E-01
Dentate gyrus	-0.019	0.010	-1.887	5.91E-02
Induseum griseum	-0.038	0.021	-1.792	7.32E-02
Entorhinal area, lateral part	0.004	0.005	0.730	4.65E-01
Entorhinal area, medial part	0.013	0.005	2.717	6.59E-03
Parasubiculum	-0.022	0.012	-1.754	7.94E-02
Postsubiculum	0.009	0.005	1.617	1.06E-01
Presubiculum	-0.002	0.005	-0.357	7.21E-01
Subiculum	-0.015	0.006	-2.409	1.60E-02
Prosubiculum	0.007	0.005	1.347	1.78E-01
Claustrum	0.014	0.007	1.993	4.62E-02
Endopiriform nucleus, dorsal part	0.034	0.010	3.312	9.27E-04
Endopiriform nucleus, ventral part	0.009	0.009	0.997	3.19E-01
Lateral amygdalar nucleus	-0.026	0.006	-4.156	3.23E-05
Basolateral amygdalar nucleus, anterior part	0.005	0.008	0.651	5.15E-01
Basolateral amygdalar nucleus, posterior part	-0.004	0.007	-0.628	5.30E-01
Basolateral amygdalar nucleus, ventral part	0.015	0.012	1.284	1.99E-01
Basomedial amygdalar nucleus, anterior part	0.012	0.020	0.622	5.34E-01
Basomedial amygdalar nucleus, posterior part	0.004	0.012	0.330	7.41E-01
Posterior amygdalar nucleus	-0.004	0.017	-0.233	8.16E-01
Caudoputamen	-0.010	0.006	-1.593	1.11E-01
Nucleus accumbens	0.023	0.010	2.239	2.52E-02
Fundus of striatum	0.004	0.011	0.379	7.04E-01
Olfactory tubercle	-0.009	0.008	-1.117	2.64E-01
Lateral septal nucleus	0.023	0.013	1.853	6.39E-02
Septofimbrial nucleus	0.003	0.020	0.161	8.72E-01
Anterior amygdalar area	-0.024	0.017	-1.395	1.63E-01
Central amygdalar nucleus, capsular part	-0.033	0.010	-3.416	6.36E-04
Central amygdalar nucleus, lateral part	-0.013	0.011	-1.197	2.31E-01
Central amygdalar nucleus, medial part	0.005	0.017	0.290	7.72E-01
Intercalated amygdalar nucleus	-0.004	0.015	-0.255	7.99E-01

Medial amygdalar nucleus	-0.005	0.026	-0.208	8.35E-01
Globus pallidus, external segment	-0.016	0.011	-1.452	1.46E-01
Globus pallidus, internal segment	0.010	0.019	0.499	6.18E-01
Substantia innominata	-0.008	0.011	-0.732	4.64E-01
Magnocellular nucleus	-0.035	0.012	-2.855	4.30E-03
Medial septal nucleus	-0.002	0.007	-0.277	7.82E-01
Diagonal band nucleus	-0.017	0.006	-2.780	5.44E-03
Triangular nucleus of septum	-0.022	0.019	-1.149	2.51E-01
Bed nuclei of the stria terminalis	0.006	0.011	0.586	5.58E-01
Ventral anterior,lateral complex of the thalamus	0.018	0.048	0.376	7.07E-01
Ventral medial nucleus of the thalamus	-0.013	0.017	-0.772	4.40E-01
Ventral posterior complex of the thalamus	-0.006	0.012	-0.508	6.11E-01
Subparafascicular nucleus	-0.001	0.020	-0.027	9.78E-01
Subparafascicular area	-0.009	0.032	-0.289	7.73E-01
Medial geniculate complex	-0.047	0.010	-4.678	2.90E-06
Lateral geniculate complex	-0.024	0.005	-4.685	2.80E-06
Lateral posterior nucleus of the thalamus	-0.025	0.009	-2.823	4.76E-03
Posterior complex of the thalamus	-0.047	0.009	-4.984	6.23E-07
Posterior limiting nucleus of the thalamus	-0.035	0.006	-5.460	4.77E-08
Suprageniculate nucleus	-0.044	0.009	-5.056	4.28E-07
Anteroventral nucleus of thalamus	-0.012	0.022	-0.530	5.96E-01
Anteromedial nucleus	0.033	0.030	1.083	2.79E-01
Anterodorsal nucleus	-0.034	0.013	-2.628	8.59E-03
Interanterodorsal nucleus of the thalamus	0.047	0.023	2.089	3.67E-02
Lateral dorsal nucleus of thalamus	-0.020	0.012	-1.625	1.04E-01
Intermediodorsal nucleus of the thalamus	-0.018	0.020	-0.880	3.79E-01
Mediodorsal nucleus of thalamus	-0.008	0.011	-0.717	4.73E-01
Submedial nucleus of the thalamus	-0.074	0.023	-3.258	1.12E-03
Perireunensis nucleus	-0.011	0.016	-0.657	5.11E-01
Paraventricular nucleus of the thalamus	-0.020	0.012	-1.707	8.78E-02
Parataenial nucleus	-0.005	0.011	-0.475	6.34E-01

Nucleus of reuniens	-0.014	0.015	-0.981	3.27E-01
Central medial nucleus of the thalamus	0.020	0.022	0.886	3.76E-01
Paracentral nucleus	-0.047	0.018	-2.610	9.05E-03
Central lateral nucleus of the thalamus	-0.004	0.012	-0.326	7.44E-01
Parafascicular nucleus	-0.012	0.010	-1.206	2.28E-01
Reticular nucleus of the thalamus	-0.023	0.011	-2.037	4.17E-02
Medial habenula	-0.074	0.014	-5.371	7.81E-08
Lateral habenula	-0.017	0.014	-1.254	2.10E-01
Paraventricular hypothalamic nucleus	0.017	0.015	1.159	2.47E-01
Periventricular hypothalamic nucleus	-0.011	0.018	-0.605	5.45E-01
Arcuate hypothalamic nucleus	-0.030	0.027	-1.111	2.67E-01
Anterodorsal preoptic nucleus	-0.004	0.014	-0.308	7.58E-01
Anteroventral periventricular nucleus	0.002	0.014	0.135	8.92E-01
Dorsomedial hypothalamic nucleus	-0.014	0.021	-0.659	5.10E-01
Medial preoptic area	0.004	0.009	0.463	6.43E-01
Subparaventricular zone	0.013	0.025	0.512	6.09E-01
Anterior hypothalamic nucleus	0.009	0.016	0.605	5.45E-01
Supramammillary nucleus	-0.050	0.046	-1.095	2.73E-01
Tuberomammillary nucleus	-0.002	0.039	-0.051	9.59E-01
Medial preoptic nucleus	-0.012	0.019	-0.618	5.37E-01
Dorsal premammillary nucleus	-0.058	0.042	-1.375	1.69E-01
Ventral premammillary nucleus	-0.032	0.055	-0.581	5.61E-01
Ventromedial hypothalamic nucleus	0.006	0.023	0.256	7.98E-01
Posterior hypothalamic nucleus	-0.026	0.025	-1.006	3.15E-01
Lateral hypothalamic area	-0.007	0.014	-0.519	6.04E-01
Lateral preoptic area	0.007	0.009	0.816	4.15E-01
Parasubthalamic nucleus	-0.005	0.033	-0.164	8.70E-01
Retrochiasmatic area	0.029	0.027	1.098	2.72E-01
Subthalamic nucleus	-0.014	0.027	-0.516	6.06E-01
Tuberal nucleus	0.001	0.027	0.037	9.70E-01
Zona incerta	-0.002	0.010	-0.223	8.23E-01

Superior colliculus, dorsal part	-0.005	0.006	-0.727	4.67E-01
Inferior colliculus, central part	-0.015	0.010	-1.579	1.14E-01
Inferior colliculus, dorsal part	-0.024	0.008	-3.001	2.69E-03
Inferior colliculus, external part	-0.018	0.009	-2.104	3.53E-02
Substantia nigra, reticular part	-0.037	0.011	-3.365	7.64E-04
Ventral tegmental area	-0.029	0.037	-0.782	4.34E-01
Midbrain reticular nucleus	-0.017	0.007	-2.312	2.08E-02
Superior colliculus, ventral part	-0.015	0.006	-2.616	8.90E-03
Periaqueductal gray	-0.013	0.006	-2.026	4.27E-02
Anterior pretectal nucleus	-0.019	0.011	-1.675	9.40E-02
Nucleus of the optic tract	-0.033	0.011	-3.038	2.38E-03
Nucleus of the posterior commissure	-0.021	0.016	-1.280	2.00E-01
Posterior pretectal nucleus	-0.026	0.007	-3.482	4.98E-04
Cuneiform nucleus	-0.009	0.007	-1.346	1.78E-01
Red nucleus	-0.009	0.018	-0.513	6.08E-01
Substantia nigra, compact part	-0.012	0.016	-0.755	4.50E-01
Pedunculopontine nucleus	-0.021	0.006	-3.831	1.27E-04
Dorsal nucleus raphe	-0.028	0.020	-1.400	1.61E-01
Nucleus of the lateral lemniscus	-0.009	0.013	-0.689	4.91E-01
Principal sensory nucleus of the trigeminal	0.033	0.015	2.207	2.73E-02
Parabrachial nucleus	-0.037	0.008	-4.803	1.57E-06
Superior olivary complex	-0.035	0.019	-1.843	6.54E-02
Dorsal tegmental nucleus	-0.053	0.016	-3.352	8.01E-04
Pontine central gray	-0.050	0.009	-5.269	1.37E-07
Pontine gray	0.034	0.039	0.873	3.83E-01
Supratrigeminal nucleus	-0.034	0.009	-3.636	2.77E-04
Tegmental reticular nucleus	-0.018	0.054	-0.329	7.42E-01
Motor nucleus of trigeminal	-0.002	0.014	-0.151	8.80E-01
Superior central nucleus raphe	-0.010	0.038	-0.263	7.93E-01
Laterodorsal tegmental nucleus	-0.037	0.013	-2.959	3.09E-03
Nucleus incertus	-0.025	0.012	-2.095	3.62E-02

Pontine reticular nucleus	-0.009	0.012	-0.800	4.24E-01
Dorsal cochlear nucleus	-0.013	0.012	-1.096	2.73E-01
Ventral cochlear nucleus	-0.022	0.014	-1.534	1.25E-01
Cuneate nucleus	-0.007	0.022	-0.306	7.60E-01
External cuneate nucleus	-0.015	0.014	-1.074	2.83E-01
Nucleus of the trapezoid body	-0.025	0.040	-0.634	5.26E-01
Nucleus of the solitary tract	-0.055	0.013	-4.103	4.07E-05
Spinal nucleus of the trigeminal	-0.019	0.011	-1.727	8.42E-02
Facial motor nucleus	0.006	0.017	0.332	7.40E-01
Dorsal motor nucleus of the vagus nerve	-0.053	0.015	-3.402	6.69E-04
Gigantocellular reticular nucleus	0.025	0.011	2.220	2.64E-02
Inferior olivary complex	-0.011	0.018	-0.619	5.36E-01
Intermediate reticular nucleus	-0.019	0.011	-1.770	7.67E-02
Lateral reticular nucleus	0.028	0.019	1.511	1.31E-01
Magnocellular reticular nucleus	0.050	0.032	1.555	1.20E-01
Medullary reticular nucleus	-0.028	0.013	-2.202	2.77E-02
Parvicellular reticular nucleus	-0.019	0.010	-1.949	5.13E-02
Paragigantocellular reticular nucleus	0.001	0.008	0.103	9.18E-01
Nucleus prepositus	0.012	0.012	1.014	3.11E-01
Lateral vestibular nucleus	-0.007	0.013	-0.519	6.04E-01
Medial vestibular nucleus	-0.034	0.006	-5.611	2.01E-08
Spinal vestibular nucleus	-0.007	0.008	-0.849	3.96E-01
Superior vestibular nucleus	-0.021	0.021	-0.986	3.24E-01
Hypoglossal nucleus	-0.029	0.014	-2.165	3.04E-02
Nucleus raphe magnus	0.012	0.026	0.460	6.46E-01

Supplementary Data Table 15: GLM coefficient estimates (**Figure 6G**, **J**). The total number of Fos$^+$ cells in each brain region was modeled as ***Counts ~ ChR2 + ln(Total Counts)*** using a negative binomial link function (*N* = 15 mice).

Brain region name	**YFP - ChR2 estimate**	**YFP - ChR2 std error**

Frontal pole	-1.325	0.620
Primary motor area	0.505	0.177
Secondary motor area	0.419	0.139
Primary somatosensory area, nose	0.441	0.327
Primary somatosensory area, barrel field	0.568	0.265
Primary somatosensory area, lower limb	0.509	0.245
Primary somatosensory area, mouth	0.326	0.360
Primary somatosensory area, upper limb	0.414	0.263
Primary somatosensory area, trunk	0.239	0.201
Supplemental somatosensory area	0.444	0.210
Gustatory areas	0.149	0.229
Visceral area	0.195	0.236
Dorsal auditory area	0.485	0.293
Primary auditory area	0.319	0.262
Posterior auditory area	-0.055	0.384
Ventral auditory area	-0.152	0.285
Anterolateral visual area	0.022	0.385
Anteromedial visual area	0.147	0.365
Lateral visual area	-0.149	0.389
Primary visual area	0.007	0.428
Posterolateral visual area	0.102	0.212
Posteromedial visual area	-0.011	0.378
Anterior cingulate area, dorsal part	0.145	0.165
Anterior cingulate area, ventral part	0.049	0.227
Prelimbic area	0.264	0.275
Infralimbic area	0.274	0.161
Orbital area, lateral part	0.547	0.234
Orbital area, medial part	0.003	0.267
Orbital area, ventrolateral part	0.256	0.260
Agranular insular area, dorsal part	0.438	0.123
Agranular insular area, posterior part	0.303	0.213

Agranular insular area, ventral part	0.321	0.151
Retrosplenial area, lateral agranular part	-0.037	0.223
Retrosplenial area, dorsal part	-0.212	0.193
Retrosplenial area, ventral part	-0.040	0.190
Rostrolateral visual area	0.152	0.307
Temporal association areas	-0.234	0.139
Perirhinal area	-0.044	0.184
Ectorhinal area	-0.011	0.234
Anterior olfactory nucleus	0.550	0.190
Taenia tecta, dorsal part	0.218	0.154
Taenia tecta, ventral part	0.210	0.384
Dorsal peduncular area	0.418	0.212
Piriform area	0.300	0.262
Nucleus of the lateral olfactory tract	-0.295	0.749
Cortical amygdalar area, anterior part	-0.212	0.438
Cortical amygdalar area, posterior part	0.033	0.373
Piriform,amygdalar area	0.153	0.262
Postpiriform transition area	-0.021	0.298
Field c a1	0.207	0.176
Field c a2	0.366	0.270
Field c a3	0.204	0.191
Dentate gyrus	-0.181	0.312
Induseum griseum	-0.540	0.634
Entorhinal area, lateral part	0.071	0.153
Entorhinal area, medial part	-0.025	0.169
Parasubiculum	-0.565	0.406
Postsubiculum	0.094	0.177
Presubiculum	-0.233	0.156
Subiculum	-0.258	0.235
Prosubiculum	-0.184	0.131
Claustrum	0.177	0.214

Endopiriform nucleus, dorsal part	0.396	0.313
Endopiriform nucleus, ventral part	0.135	0.211
Lateral amygdalar nucleus	-0.535	0.238
Basolateral amygdalar nucleus, anterior part	-0.175	0.192
Basolateral amygdalar nucleus, posterior part	-0.209	0.158
Basolateral amygdalar nucleus, ventral part	0.164	0.228
Basomedial amygdalar nucleus, anterior part	-0.068	0.422
Basomedial amygdalar nucleus, posterior part	-0.165	0.257
Posterior amygdalar nucleus	-0.344	0.380
Caudoputamen	-0.165	0.219
Nucleus accumbens	0.225	0.330
Fundus of striatum	0.276	0.262
Olfactory tubercle	0.107	0.276
Lateral septal nucleus	-0.054	0.340
Septofimbrial nucleus	-0.805	0.522
Anterior amygdalar area	-0.580	0.457
Central amygdalar nucleus, capsular part	-0.716	0.378
Central amygdalar nucleus, lateral part	-0.049	0.299
Central amygdalar nucleus, medial part	-0.223	0.368
Intercalated amygdalar nucleus	-0.043	0.342
Medial amygdalar nucleus	-0.541	0.513
Globus pallidus, external segment	-0.060	0.353
Globus pallidus, internal segment	0.343	0.425
Substantia innominata	-0.017	0.292
Magnocellular nucleus	-0.528	0.462
Medial septal nucleus	0.084	0.185
Diagonal band nucleus	-0.216	0.233
Triangular nucleus of septum	-1.309	0.572
Bed nuclei of the stria terminalis	0.033	0.277

Ventral anterior,lateral complex of the thalamus	-1.971	0.726
Ventral medial nucleus of the thalamus	0.021	0.407
Ventral posterior complex of the thalamus	-0.413	0.313
Subparafascicular nucleus	-0.718	0.401
Subparafascicular area	-0.895	0.717
Medial geniculate complex	-1.067	0.525
Lateral geniculate complex	-0.646	0.224
Lateral posterior nucleus of the thalamus	-0.884	0.257
Posterior complex of the thalamus	-1.129	0.531
Posterior limiting nucleus of the thalamus	-0.744	0.280
Suprageniculate nucleus	-0.927	0.451
Anteroventral nucleus of thalamus	-1.351	0.611
Anteromedial nucleus	-0.970	0.608
Anterodorsal nucleus	-1.089	0.442
Interanterodorsal nucleus of the thalamus	-0.517	0.453
Lateral dorsal nucleus of thalamus	-0.717	0.329
Intermediodorsal nucleus of the thalamus	-0.474	0.499
Mediodorsal nucleus of thalamus	-0.408	0.302
Submedial nucleus of the thalamus	-1.617	0.787
Perireunensis nucleus	0.010	0.394
Paraventricular nucleus of the thalamus	-0.664	0.345
Parataenial nucleus	-0.547	0.307
Nucleus of reuniens	-0.072	0.413
Central medial nucleus of the thalamus	-0.227	0.524
Paracentral nucleus	-0.181	0.686
Central lateral nucleus of the thalamus	-0.693	0.278
Parafascicular nucleus	-0.259	0.251
Reticular nucleus of the thalamus	-0.684	0.345
Medial habenula	-1.942	0.640
Lateral habenula	-0.530	0.404
Paraventricular hypothalamic nucleus	-0.115	0.377

Periventricular hypothalamic nucleus	-0.263	0.483
Arcuate hypothalamic nucleus	-1.007	0.733
Anterodorsal preoptic nucleus	-0.228	0.312
Anteroventral periventricular nucleus	-0.015	0.354
Dorsomedial hypothalamic nucleus	-0.195	0.542
Medial preoptic area	-0.051	0.235
Subparaventricular zone	-0.074	0.546
Anterior hypothalamic nucleus	0.070	0.348
Supramammillary nucleus	-1.702	0.863
Tuberomammillary nucleus	-1.343	0.628
Medial preoptic nucleus	-0.361	0.465
Dorsal premammillary nucleus	-1.607	0.848
Ventral premammillary nucleus	-1.346	0.953
Ventromedial hypothalamic nucleus	-0.103	0.502
Posterior hypothalamic nucleus	-1.059	0.581
Lateral hypothalamic area	-0.214	0.328
Lateral preoptic area	0.192	0.220
Parasubthalamic nucleus	-0.236	0.630
Retrochiasmatic area	0.091	0.595
Subthalamic nucleus	0.223	0.517
Tuberal nucleus	-0.236	0.510
Zona incerta	0.218	0.254
Superior colliculus, dorsal part	-0.160	0.211
Inferior colliculus, central part	0.387	0.293
Inferior colliculus, dorsal part	0.110	0.312
Inferior colliculus, external part	0.106	0.295
Substantia nigra, reticular part	-0.320	0.436
Ventral tegmental area	-0.514	0.693
Midbrain reticular nucleus	-0.296	0.222
Superior colliculus, ventral part	-0.125	0.198
Periaqueductal gray	-0.415	0.168

Anterior pretectal nucleus	-0.528	0.336
Nucleus of the optic tract	-0.840	0.436
Nucleus of the posterior commissure	-0.848	0.421
Posterior pretectal nucleus	-0.769	0.247
Cuneiform nucleus	-0.458	0.160
Red nucleus	0.068	0.425
Substantia nigra, compact part	-0.019	0.363
Pedunculopontine nucleus	-0.311	0.231
Dorsal nucleus raphe	-0.332	0.601
Nucleus of the lateral lemniscus	-0.449	0.361
Principal sensory nucleus of the trigeminal	0.047	0.332
Parabrachial nucleus	-0.960	0.408
Superior olivary complex	0.055	0.421
Dorsal tegmental nucleus	-0.707	0.771
Pontine central gray	-0.953	0.587
Pontine gray	-0.122	0.720
Supratrigeminal nucleus	-0.613	0.462
Tegmental reticular nucleus	0.714	0.822
Motor nucleus of trigeminal	0.093	0.368
Superior central nucleus raphe	0.902	0.677
Laterodorsal tegmental nucleus	-0.384	0.578
Nucleus incertus	-0.288	0.441
Pontine reticular nucleus	-0.357	0.298
Dorsal cochlear nucleus	0.489	0.294
Ventral cochlear nucleus	0.428	0.445
Cuneate nucleus	-0.378	0.421
External cuneate nucleus	-0.181	0.371
Nucleus of the trapezoid body	-1.137	0.771
Nucleus of the solitary tract	-1.367	0.775
Spinal nucleus of the trigeminal	-0.285	0.391
Facial motor nucleus	-0.342	0.439

Dorsal motor nucleus of the vagus nerve	-1.387	0.847
Gigantocellular reticular nucleus	-0.013	0.317
Inferior olivary complex	-0.442	0.442
Intermediate reticular nucleus	-0.417	0.483
Lateral reticular nucleus	-0.718	0.453
Magnocellular reticular nucleus	-0.596	0.559
Medullary reticular nucleus	-0.798	0.469
Parvicellular reticular nucleus	-0.315	0.413
Paragigantocellular reticular nucleus	-0.206	0.234
Nucleus prepositus	-0.060	0.320
Lateral vestibular nucleus	0.211	0.282
Medial vestibular nucleus	-0.672	0.299
Spinal vestibular nucleus	-0.092	0.236
Superior vestibular nucleus	0.288	0.538
Hypoglossal nucleus	-0.549	0.639
Nucleus raphe magnus	0.419	0.611

References

1. Breslau, N., and Davis, G.C. (1986). Chronic stress and major depression. Arch. Gen. Psychiatry *43*, 309–314.

2. McEwen, B.S., and Akil, H. (2020). Revisiting the Stress Concept: Implications for Affective Disorders. J. Neurosci. *40*, 12–21.

3. Daviu, N., Bruchas, M.R., Moghaddam, B., Sandi, C., and Beyeler, A. (2019). Neurobiological links between stress and anxiety. Neurobiol Stress *11*, 100191.

4. Berton, O., McClung, C.A., Dileone, R.J., Krishnan, V., Renthal, W., Russo, S.J., Graham, D., Tsankova, N.M., Bolanos, C.A., Rios, M., et al. (2006). Essential role of BDNF in the mesolimbic dopamine pathway in social defeat stress. Science *311*, 864–868.

5. Krishnan, V., Han, M.-H., Graham, D.L., Berton, O., Renthal, W., Russo, S.J., Laplant, Q., Graham, A., Lutter, M., Lagace, D.C., et al. (2007). Molecular adaptations underlying susceptibility and resistance to social defeat in brain reward regions. Cell *131*, 391–404.

6. Yohn, C.N., Dieterich, A., Bazer, A.S., Maita, I., Giedraitis, M., and Samuels, B.A. (2019). Chronic non-discriminatory social defeat is an effective chronic stress paradigm for both male and female mice. Neuropsychopharmacology *44*, 2220–2229.

7. Kudryavtseva, N.N., Bakshtanovskaya, I.V., and Koryakina, L.A. (1991). Social model of depression in mice of C57BL/6J strain. Pharmacol. Biochem. Behav. *38*, 315–320.

8. Rygula, R., Abumaria, N., Flügge, G., Hiemke, C., Fuchs, E., Rüther, E., and Havemann-Reinecke, U. (2006). Citalopram counteracts depressive-like symptoms evoked by chronic social stress in rats. Behav. Pharmacol. *17*, 19–29.

9. Avgustinovich, D.F., Kovalenko, I.L., and Kudryavtseva, N.N. (2005). A model of anxious depression: persistence of behavioral pathology. Neurosci. Behav. Physiol. *35*, 917–924.

10. Chaudhury, D., Walsh, J.J., Friedman, A.K., Juarez, B., Ku, S.M., Koo, J.W., Ferguson, D., Tsai, H.-C., Pomeranz, L., Christoffel, D.J., et al. (2013). Rapid regulation of depression-related behaviours by control of midbrain dopamine neurons. Nature *493*, 532–536.

11. Cao, J.-L., Covington, H.E., 3rd, Friedman, A.K., Wilkinson, M.B., Walsh, J.J., Cooper, D.C., Nestler, E.J., and Han, M.-H. (2010). Mesolimbic dopamine neurons in the brain reward circuit mediate susceptibility to social defeat and antidepressant action. J. Neurosci. *30*, 16453–16458.

12. Diaz, V., and Lin, D. (2019). Neural circuits for coping with social defeat. Curr. Opin. Neurobiol. *60*, 99–107.

13. McLaughlin, J.P., Li, S., Valdez, J., Chavkin, T.A., and Chavkin, C. (2006). Social defeat stress-induced behavioral responses are mediated by the endogenous kappa opioid system. Neuropsychopharmacology *31*, 1241–1248.

14. Larrieu, T., Cherix, A., Duque, A., Rodrigues, J., Lei, H., Gruetter, R., and Sandi, C. (2017).

Hierarchical Status Predicts Behavioral Vulnerability and Nucleus Accumbens Metabolic Profile Following Chronic Social Defeat Stress. Curr. Biol. *27*, 2202–2210.e4.

15. Duclot, F., and Kabbaj, M. (2013). Individual differences in novelty seeking predict subsequent vulnerability to social defeat through a differential epigenetic regulation of brain-derived neurotrophic factor expression. J. Neurosci. *33*, 11048–11060.

16. Sandi, C., and Richter-Levin, G. (2009). From high anxiety trait to depression: a neurocognitive hypothesis. Trends Neurosci. *32*, 312–320.

17. Henckens, M.J.A.G., Klumpers, F., Everaerd, D., Kooijman, S.C., van Wingen, G.A., and Fernández, G. (2016). Interindividual differences in stress sensitivity: basal and stress-induced cortisol levels differentially predict neural vigilance processing under stress. Soc. Cogn. Affect. Neurosci. *11*, 663–673.

18. Nasca, C., Menard, C., Hodes, G., Bigio, B., Pena, C., Lorsch, Z., Zelli, D., Ferris, A., Kana, V., Purushothaman, I., et al. (2019). Multidimensional Predictors of Susceptibility and Resilience to Social Defeat Stress. Biol. Psychiatry *86*, 483–491.

19. Radwan, B., Jansen, G., and Chaudhury, D. (2020). Abnormal Sleep Signals Vulnerability to Chronic Social Defeat Stress. Front. Neurosci. *14*, 610655.

20. Cerniauskas, I., Winterer, J., de Jong, J.W., Lukacsovich, D., Yang, H., Khan, F., Peck, J.R., Obayashi, S.K., Lilascharoen, V., Lim, B.K., et al. (2019). Chronic Stress Induces Activity, Synaptic, and Transcriptional Remodeling of the Lateral Habenula Associated with Deficits in Motivated Behaviors. Neuron *104*, 899–915.e8.

21. Friedman, A.K., Walsh, J.J., Juarez, B., Ku, S.M., Chaudhury, D., Wang, J., Li, X., Dietz, D.M., Pan, N., Vialou, V.F., et al. (2014). Enhancing depression mechanisms in midbrain dopamine neurons achieves homeostatic resilience. Science *344*, 313–319.

22. LeClair, K.B., Chan, K.L., Kaster, M.P., Parise, L.F., Burnett, C.J., and Russo, S.J. (2021). Individual history of winning and hierarchy landscape influence stress susceptibility in mice. Elife *10*. 10.7554/eLife.71401.

23. Lemos, J.C., Roth, C.A., Messinger, D.I., Gill, H.K., Phillips, P.E.M., and Chavkin, C. (2012). Repeated stress dysregulates κ-opioid receptor signaling in the dorsal raphe through a p38α MAPK-dependent mechanism. J. Neurosci. *32*, 12325–12336.

24. Lemos, J.C., Wanat, M.J., Smith, J.S., Reyes, B.A.S., Hollon, N.G., Van Bockstaele, E.J., Chavkin, C., and Phillips, P.E.M. (2012). Severe stress switches CRF action in the nucleus accumbens from appetitive to aversive. Nature *490*, 402–406.

25. Nygard, S.K., Hourguettes, N.J., Sobczak, G.G., Carlezon, W.A., and Bruchas, M.R. (2016). Stress-Induced Reinstatement of Nicotine Preference Requires Dynorphin/Kappa Opioid Activity in the Basolateral Amygdala. J. Neurosci. *36*, 9937–9948.

26. Willmore, L., Cameron, C., Yang, J., Witten, I.B., and Falkner, A.L. (2022). Behavioural and dopaminergic signatures of resilience. Nature *611*, 124–132.

27. Schultz, W., Dayan, P., and Montague, P.R. (1997). A neural substrate of prediction and reward. Science *275*, 1593–1599.

28. Cohen, J.Y., Haesler, S., Vong, L., Lowell, B.B., and Uchida, N. (2012). Neuron-type-specific signals for reward and punishment in the ventral tegmental area. Nature *482*, 85–88.

29. Steinberg, E.E., Keiflin, R., Boivin, J.R., Witten, I.B., Deisseroth, K., and Janak, P.H. (2013). A causal link between prediction errors, dopamine neurons and learning. Nat. Neurosci. *16*, 966–973.

30. Tsutsui-Kimura, I., Matsumoto, H., Akiti, K., Yamada, M.M., Uchida, N., and Watabe-Uchida, M. (2020). Distinct temporal difference error signals in dopamine axons in three regions of the striatum in a decision-making task. Elife *9*. 10.7554/eLife.62390.

31. Witten, I.B., Steinberg, E.E., Lee, S.Y., Davidson, T.J., Zalocusky, K.A., Brodsky, M., Yizhar, O., Cho, S.L., Gong, S., Ramakrishnan, C., et al. (2011). Recombinase-driver rat lines: tools, techniques, and optogenetic application to dopamine-mediated reinforcement. Neuron *72*, 721–733.

32. Matsumoto, M., and Hikosaka, O. (2007). Lateral habenula as a source of negative reward signals in dopamine neurons. Nature *447*, 1111–1115.

33. Li, H., Pullmann, D., and Jhou, T.C. The entopeduncular nucleus drives lateral habenula responses to negative but not positive or neutral affective stimuli. 10.1101/408963.

34. Hu, H., Cui, Y., and Yang, Y. (2020). Circuits and functions of the lateral habenula in health and in disease. Nat. Rev. Neurosci. *21*, 277–295.

35. Stamatakis, A.M., and Stuber, G.D. (2012). Activation of lateral habenula inputs to the ventral midbrain promotes behavioral avoidance. Nat. Neurosci. *15*, 1105–1107.

36. Wang, D., Li, Y., Feng, Q., Guo, Q., Zhou, J., and Luo, M. (2017). Learning shapes the aversion and reward responses of lateral habenula neurons. Elife *6*, e23045.

37. Yang, Y., Cui, Y., Sang, K., Dong, Y., Ni, Z., Ma, S., and Hu, H. (2018). Ketamine blocks bursting in the lateral habenula to rapidly relieve depression. Nature *554*, 317–322.

38. Wang, D., Li, A., Dong, K., Li, H., Guo, Y., Zhang, X., Cai, M., Li, H., Zhao, G., and Yang, Q. (2021). Lateral hypothalamus orexinergic inputs to lateral habenula modulate maladaptation after social defeat stress. Neurobiol Stress *14*, 100298.

39. Fan, Z., Chang, J., Liang, Y., Zhu, H., Zhang, C., Zheng, D., Wang, J., Xu, Y., Li, Q.-J., and Hu, H. (2023). Neural mechanism underlying depressive-like state associated with social status loss. Cell *186*, 560–576.e17.

40. Park, H., Rhee, J., Park, K., Han, J.-S., Malinow, R., and Chung, C. (2017). Exposure to Stressors Facilitates Long-Term Synaptic Potentiation in the Lateral Habenula. J. Neurosci. *37*, 6021–6030.

41. Li, B., Piriz, J., Mirrione, M., Chung, C., Proulx, C.D., Schulz, D., Henn, F., and Malinow, R. (2011). Synaptic potentiation onto habenula neurons in the learned helplessness model of depression. Nature *470*, 535–539.

42. Nuno-Perez, A., Trusel, M., Lalive, A.L., Congiu, M., Gastaldo, D., Tchenio, A., Lecca, S., Soiza-Reilly, M., Bagni, C., and Mameli, M. (2021). Stress undermines reward-guided

cognitive performance through synaptic depression in the lateral habenula. Neuron *109*, 947–956.e5.

43. Li, K., Zhou, T., Liao, L., Yang, Z., Wong, C., Henn, F., Malinow, R., Yates, J.R., 3rd, and Hu, H. (2013). βCaMKII in lateral habenula mediates core symptoms of depression. Science *341*, 1016–1020.

44. Winter, C., Vollmayr, B., Djodari-Irani, A., Klein, J., and Sartorius, A. (2011). Pharmacological inhibition of the lateral habenula improves depressive-like behavior in an animal model of treatment resistant depression. Behav. Brain Res. *216*, 463–465.

45. Amat, J., Sparks, P.D., Matus-Amat, P., Griggs, J., Watkins, L.R., and Maier, S.F. (2001). The role of the habenular complex in the elevation of dorsal raphe nucleus serotonin and the changes in the behavioral responses produced by uncontrollable stress. Brain Res. *917*, 118–126.

46. Tsankova, N.M., Berton, O., Renthal, W., Kumar, A., Neve, R.L., and Nestler, E.J. (2006). Sustained hippocampal chromatin regulation in a mouse model of depression and antidepressant action. Nat. Neurosci. *9*, 519–525.

47. Golden, S.A., Covington, H.E., 3rd, Berton, O., and Russo, S.J. (2011). A standardized protocol for repeated social defeat stress in mice. Nat. Protoc. *6*, 1183–1191.

48. McAllister, B.B., Pochakom, A., Fu, S., and Dyck, R.H. (2020). Effects of social defeat stress and fluoxetine treatment on neurogenesis and behavior in mice that lack zinc transporter 3 (ZnT3) and vesicular zinc. Hippocampus *30*, 623–637.

49. Murra, D., Hilde, K.L., Fitzpatrick, A., Maras, P.M., Watson, S.J., and Akil, H. (2022). Characterizing the behavioral and neuroendocrine features of susceptibility and resilience to social stress. Neurobiol Stress *17*, 100437.

50. Ayash, S., Schmitt, U., and Müller, M.B. (2020). Chronic social defeat-induced social avoidance as a proxy of stress resilience in mice involves conditioned learning. J. Psychiatr. Res. *120*, 64–71.

51. Li, L., Durand-de Cuttoli, R., Aubry, A.V., Burnett, C.J., Cathomas, F., Parise, L.F., Chan, K.L., Morel, C., Yuan, C., Shimo, Y., et al. (2022). Social trauma engages lateral septum circuitry to occlude social reward. Nature. 10.1038/s41586-022-05484-5.

52. Pisano, T.J., Hoag, A.T., Dhanerawala, Z.M., Guariglia, S.R., Jung, C., Boele, H.-J., Seagraves, K.M., Verpeut, J.L., and Wang, S.S.-H. (2022). Automated high-throughput mouse transsynaptic viral tracing using iDISCO+ tissue clearing, light-sheet microscopy, and BrainPipe. STAR Protoc *3*, 101289.

53. Renier, N., Adams, E.L., Kirst, C., Wu, Z., Azevedo, R., Kohl, J., Autry, A.E., Kadiri, L., Umadevi Venkataraju, K., Zhou, Y., et al. (2016). Mapping of Brain Activity by Automated Volume Analysis of Immediate Early Genes. Cell *165*, 1789–1802.

54. Zimmerman, C.A., Pan-Vazquez, A., Wu, B., Keppler, E.F., Guthman, E.M., Fetcho, R.N., Bolkan, S.S., McMannon, B., Lee, J., Hoag, A.T., et al. (2023). A neural mechanism for learning from delayed postingestive feedback. bioRxiv, 2023.10.06.561214. 10.1101/2023.10.06.561214.

55. Wang, Q., Ding, S.-L., Li, Y., Royall, J., Feng, D., Lesnar, P., Graddis, N., Naeemi, M., Facer, B., Ho, A., et al. (2020). The Allen Mouse Brain Common Coordinate Framework: A 3D Reference Atlas. Cell *181*, 936–953.e20.

56. Lee, H., and Hikosaka, O. (2022). Lateral habenula neurons signal step-by-step changes of reward prediction. iScience, 105440.

57. Matsumoto, M., and Hikosaka, O. (2009). Representation of negative motivational value in the primate lateral habenula. Nat. Neurosci. *12*, 77–84.

58. Hennigan, K., D'Ardenne, K., and McClure, S.M. (2015). Distinct midbrain and habenula pathways are involved in processing aversive events in humans. J. Neurosci. *35*, 198–208.

59. Liu, H., Rastogi, A., Narain, P., Xu, Q., Sabanovic, M., Alhammadi, A.D., Guo, L., Cao, J.-L., Zhang, H., Aqel, H., et al. (2021). Blunted diurnal firing in lateral habenula projections to dorsal raphe nucleus and delayed photoentrainment in stress-susceptible mice. PLoS Biol. *19*, e3000709.

60. Li, Z.-L., Wang, Y., Zou, H.-W., Jing, X.-Y., Liu, Y.-J., and Li, L.-F. (2021). GABA(B) receptors within the lateral habenula modulate stress resilience and vulnerability in mice. Physiol. Behav. *230*, 113311.

61. Ma, S., Chen, M., Jiang, Y., Xiang, X., Wang, S., Wu, Z., Li, S., Cui, Y., Wang, J., Zhu, Y., et al. (2023). Sustained antidepressant effect of ketamine through NMDAR trapping in the LHb. Nature *622*, 802–809.

62. Murra, D., Hilde, K.L., Khalil, H., Watson, S.J., and Akil, H. (2023). Patterns of Neural Activation During an Initial Social Stress Encounter are Predictive of Future Susceptibility or Resilience: A FosTRAP2 Study. bioRxiv, 2023.03.10.532130. 10.1101/2023.03.10.532130.

63. Li, H.-Y., Zhu, M.-Z., Yuan, X.-R., Guo, Z.-X., Pan, Y.-D., Li, Y.-Q., and Zhu, X.-H. (2023). A thalamic-primary auditory cortex circuit mediates resilience to stress. Cell *186*, 1352–1368.e18.

64. Lorsch, Z.S., Hamilton, P.J., Ramakrishnan, A., Parise, E.M., Salery, M., Wright, W.J., Lepack, A.E., Mews, P., Issler, O., McKenzie, A., et al. (2019). Stress resilience is promoted by a Zfp189-driven transcriptional network in prefrontal cortex. Nat. Neurosci. *22*, 1413–1423.

65. Amat, J., Paul, E., Watkins, L.R., and Maier, S.F. (2008). Activation of the ventral medial prefrontal cortex during an uncontrollable stressor reproduces both the immediate and long-term protective effects of behavioral control. Neuroscience *154*, 1178–1186.

66. Fetcho, R.N., Hall, B.S., Estrin, D.J., Walsh, A.P., Schuette, P.J., Kaminsky, J., Singh, A., Roshgodal, J., Bavley, C.C., Nadkarni, V., et al. (2023). Regulation of social interaction in mice by a frontostriatal circuit modulated by established hierarchical relationships. Nat. Commun. *14*, 2487.

67. Bagot, R.C., Parise, E.M., Peña, C.J., Zhang, H.-X., Maze, I., Chaudhury, D., Persaud, B., Cachope, R., Bolaños-Guzmán, C.A., Cheer, J.F., et al. (2015). Ventral hippocampal afferents to the nucleus accumbens regulate susceptibility to depression. Nat. Commun. *6*, 7062.

68. Kumar, S., Hultman, R., Hughes, D., Michel, N., Katz, B.M., and Dzirasa, K. (2014). Prefrontal cortex reactivity underlies trait vulnerability to chronic social defeat stress. Nat. Commun. *5*, 4537.

69. Morel, C., Montgomery, S.E., Li, L., Durand-de Cuttoli, R., Teichman, E.M., Juarez, B., Tzavaras, N., Ku, S.M., Flanigan, M.E., Cai, M., et al. (2022). Midbrain projection to the basolateral amygdala encodes anxiety-like but not depression-like behaviors. Nat. Commun. *13*, 1532.

70. Heshmati, M., Christoffel, D.J., LeClair, K., Cathomas, F., Golden, S.A., Aleyasin, H., Turecki, G., Friedman, A.K., Han, M.-H., Menard, C., et al. (2020). Depression and Social Defeat Stress Are Associated with Inhibitory Synaptic Changes in the Nucleus Accumbens. J. Neurosci. *40*, 6228–6233.

71. Jasnow, A.M., Davis, M., and Huhman, K.L. (2004). Involvement of central amygdalar and bed nucleus of the stria terminalis corticotropin-releasing factor in behavioral responses to social defeat. Behav. Neurosci. *118*, 1052–1061.

72. Markham, C.M., Norvelle, A., and Huhman, K.L. (2009). Role of the bed nucleus of the stria terminalis in the acquisition and expression of conditioned defeat in Syrian hamsters. Behav. Brain Res. *198*, 69–73.

73. Colyn, L., Venzala, E., Marco, S., Perez-Otaño, I., and Tordera, R.M. (2019). Chronic social defeat stress induces sustained synaptic structural changes in the prefrontal cortex and amygdala. Behav. Brain Res. *373*, 112079.

74. Zhuang, L., Gao, W., Chen, Y., Fang, W., Lo, H., Dai, X., Zhang, J., Chen, W., Ye, Q., Chen, X., et al. (2023). LHPP in glutamatergic neurons of the ventral hippocampus mediates depression-like behavior by dephosphorylating CaMKIIα and ERK. Biol. Psychiatry. 10.1016/j.biopsych.2023.08.026.

75. Bruchas, M.R., Land, B.B., Lemos, J.C., and Chavkin, C. (2009). CRF1-R activation of the dynorphin/kappa opioid system in the mouse basolateral amygdala mediates anxiety-like behavior. PLoS One *4*, e8528.

76. Jhou, T.C., Fields, H.L., Baxter, M.G., Saper, C.B., and Holland, P.C. (2009). The rostromedial tegmental nucleus (RMTg), a GABAergic afferent to midbrain dopamine neurons, encodes aversive stimuli and inhibits motor responses. Neuron *61*, 786–800.

77. Hong, S., Jhou, T.C., Smith, M., Saleem, K.S., and Hikosaka, O. (2011). Negative reward signals from the lateral habenula to dopamine neurons are mediated by rostromedial tegmental nucleus in primates. J. Neurosci. *31*, 11457–11471.

78. Post, R.J., Bulkin, D.A., Ebitz, R.B., Lee, V., Han, K., and Warden, M.R. (2022). Tonic activity in lateral habenula neurons acts as a neutral valence brake on reward-seeking behavior. Curr. Biol. *32*, 4325–4336.e5.

79. Christoph, G.R., Leonzio, R.J., and Wilcox, K.S. (1986). Stimulation of the lateral habenula inhibits dopamine-containing neurons in the substantia nigra and ventral tegmental area of the rat. J. Neurosci. *6*, 613–619.

80. Ji, H., and Shepard, P.D. (2007). Lateral habenula stimulation inhibits rat midbrain

dopamine neurons through a GABA(A) receptor-mediated mechanism. J. Neurosci. *27*, 6923–6930.

81. van Zessen, R., Phillips, J.L., Budygin, E.A., and Stuber, G.D. (2012). Activation of VTA GABA neurons disrupts reward consumption. Neuron *73*, 1184–1194.

82. Pollak Dorocic, I., Fürth, D., Xuan, Y., Johansson, Y., Pozzi, L., Silberberg, G., Carlén, M., and Meletis, K. (2014). A whole-brain atlas of inputs to serotonergic neurons of the dorsal and median raphe nuclei. Neuron *83*, 663–678.

83. Ogawa, S.K., Cohen, J.Y., Hwang, D., Uchida, N., and Watabe-Uchida, M. (2014). Organization of monosynaptic inputs to the serotonin and dopamine neuromodulatory systems. Cell Rep. *8*, 1105–1118.

84. Weissbourd, B., Ren, J., DeLoach, K.E., Guenthner, C.J., Miyamichi, K., and Luo, L. (2014). Presynaptic partners of dorsal raphe serotonergic and GABAergic neurons. Neuron *83*, 645–662.

85. Zhou, L., Liu, M.-Z., Li, Q., Deng, J., Mu, D., and Sun, Y.-G. (2017). Organization of Functional Long-Range Circuits Controlling the Activity of Serotonergic Neurons in the Dorsal Raphe Nucleus. Cell Rep. *18*, 3018–3032.

86. Herkenham, M., and Nauta, W.J. (1979). Efferent connections of the habenular nuclei in the rat. J. Comp. Neurol. *187*, 19–47.

87. Behzadi, G., Kalén, P., Parvopassu, F., and Wiklund, L. (1990). Afferents to the median raphe nucleus of the rat: retrograde cholera toxin and wheat germ conjugated horseradish peroxidase tracing, and selective D-[3H]aspartate labelling of possible excitatory amino acid inputs. Neuroscience *37*, 77–100.

88. Vertes, R.P., Fortin, W.J., and Crane, A.M. (1999). Projections of the median raphe nucleus in the rat. J. Comp. Neurol. *407*, 555–582.

89. Challis, C., Boulden, J., Veerakumar, A., Espallergues, J., Vassoler, F.M., Pierce, R.C., Beck, S.G., and Berton, O. (2013). Raphe GABAergic neurons mediate the acquisition of avoidance after social defeat. J. Neurosci. *33*, 13978–13988, 13988a.

90. Zheng, Z., Guo, C., Li, M., Yang, L., Liu, P., Zhang, X., Liu, Y., Guo, X., Cao, S., Dong, Y., et al. (2022). Hypothalamus-habenula potentiation encodes chronic stress experience and drives depression onset. Neuron *110*, 1400–1415.e6.

91. Tye, K.M., Mirzabekov, J.J., Warden, M.R., Ferenczi, E.A., Tsai, H.-C., Finkelstein, J., Kim, S.-Y., Adhikari, A., Thompson, K.R., Andalman, A.S., et al. (2013). Dopamine neurons modulate neural encoding and expression of depression-related behaviour. Nature *493*, 537–541.

92. Bagot, R.C., Cates, H.M., Purushothaman, I., Lorsch, Z.S., Walker, D.M., Wang, J., Huang, X., Schlüter, O.M., Maze, I., Peña, C.J., et al. (2016). Circuit-wide Transcriptional Profiling Reveals Brain Region-Specific Gene Networks Regulating Depression Susceptibility. Neuron *90*, 969–983.

93. Dombeck, D.A., Khabbaz, A.N., Collman, F., Adelman, T.L., and Tank, D.W. (2007). Imaging

large-scale neural activity with cellular resolution in awake, mobile mice. Neuron *56*, 43–57.

94. Friard, O., and Gamba, M. (2016). BORIS: a free, versatile open-source event-logging software for video/audio coding and live observations. Methods Ecol. Evol. *7*, 1325–1330.

95. Mathis, A., Mamidanna, P., Cury, K.M., Abe, T., Murthy, V.N., Mathis, M.W., and Bethge, M. (2018). DeepLabCut: markerless pose estimation of user-defined body parts with deep learning. Nat. Neurosci. *21*, 1281–1289.

96. Berman, G.J., Choi, D.M., Bialek, W., and Shaevitz, J.W. (2014). Mapping the stereotyped behaviour of freely moving fruit flies. J. R. Soc. Interface *11*. 10.1098/rsif.2014.0672.

97. Pnevmatikakis, E.A., and Giovannucci, A. (2017). NoRMCorre: An online algorithm for piecewise rigid motion correction of calcium imaging data. J. Neurosci. Methods *291*, 83–94.

98. Zhou, P., Resendez, S.L., Rodriguez-Romaguera, J., Jimenez, J.C., Neufeld, S.Q., Giovannucci, A., Friedrich, J., Pnevmatikakis, E.A., Stuber, G.D., Hen, R., et al. (2018). Efficient and accurate extraction of in vivo calcium signals from microendoscopic video data. Elife *7*. 10.7554/eLife.28728.

99. Pnevmatikakis, E.A., Soudry, D., Gao, Y., Machado, T.A., Merel, J., Pfau, D., Reardon, T., Mu, Y., Lacefield, C., Yang, W., et al. (2016). Simultaneous Denoising, Deconvolution, and Demixing of Calcium Imaging Data. Neuron *89*, 285–299.

100. Tyson, A.L., Rousseau, C.V., Niedworok, C.J., Keshavarzi, S., Tsitoura, C., Cossell, L., Strom, M., and Margrie, T.W. (2021). A deep learning algorithm for 3D cell detection in whole mouse brain image datasets. PLoS Comput. Biol. *17*, e1009074.